Efficient IMEX and consistently energy-stable methods of diffuse-interface models for incompressible three-component flows ☆

Junxiang Yang [a], Jian Wang [b], Zhijun Tan [a,c], Junseok Kim [d,*]

[a] School of Computer Science and Engineering, Sun Yat-sen University, Guangzhou 510275, China
[b] School of Mathematics and Statistic, Nanjing University of Information Science and Technology, Nanjing, 210044, China
[c] Guangdong Province Key Laboratory of Computational Science, Sun Yat-sen University, Guangzhou 510275, China
[d] Department of Mathematics, Korea University, Seoul, 02841, Republic of Korea

ARTICLE INFO

ABSTRACT

In this study, we consider the numerical approximation of incompressible three-component fluids, in which the fluid interfaces are captured by ternary Cahn–Hilliard equations and the fluid flows are governed by Navier–Stokes equations. This system includes not only nonlinear effects but also coupling among phase-field variables, velocities, and pressure. The ternary Cahn–Hilliard–Navier–Stokes system also satisfies the energy dissipation law, which is a basic physical property. For the appropriate treatment of the nonlinear and coupling terms and preservation of the energy dissipation law in a discrete version, we develop second-order time-accurate, linearly implicit-explicit (IMEX) methods using a variation of the scalar auxiliary variable (SAV) method. To improve the consistency between the original and modified energies, a simple and effective energy relaxation technique is considered. We analytically proved the unique solvability and the relaxed energy dissipation law. The proposed schemes are highly efficient for implementation because only linear elliptic equations need to be solved separately. Extensive computational experiments are performed to validate the accuracy, energy stability, and performance of the proposed method. To facilitate further study, we provide the C codes for the typical numerical simulations at http://github.com/yang521.

© 2022 Elsevier B.V. All rights reserved.

1. Introduction

The phase-field or diffuse-interface methods are powerful and efficient tools for modeling significant physical problems in materials science or fluid mechanics [1–3]. The Cahn–Hilliard (CH) equation is a typical phase-field model proposed by Cahn and Hilliard [4] for the mass-conserved spinodal decomposition of binary alloys. The main advantages of the CH equation for conservative problems with interfaces include the following: (i) The interfacial positions are easily captured by solving the governing equations; (ii) The mass conservation is naturally satisfied with the use of periodic or homogeneous Neumann boundary conditions. With the rise of interdisciplinary studies, the CH equation has been effectively applied in two-phase flow simulations [5–9], three-dimensional (3D) volume reconstruction [10], image inpainting [11], multiphase spinodal decomposition [12], and biological dynamics simulations [13,14], etc. In addition to mass conservation, the energy law is another basic property of the CH equation. Over time, the solution of the CH equation will dissipate the free energy of the system in the absence of an external force acting on it. This energy dissipation-property is in accordance with the second law of thermodynamics. To preserve the discrete version of the energy dissipation law, researchers have developed practical methods based on nonlinear temporal discretization, (e.g., convex splitting method) [15–19], and linear temporal discretization, (e.g., stabilization method [20,21], energy factorization method [22], and auxiliary variables method) [23–27].

Compared with the classical binary CH equation, the three-phase model is important because in reality, most physical phenomena have more than two components. Examples include the double emulsion formation in a microfluid device [28], multiple cell division [14],

---

and water-oil-surfactant mixtures [29,30]. Based on the two-phase CH model, Kim [31] proposed a simple ternary CH model which is a straightforward extension of the binary model. The proposed model was validated via the numerical simulation of a ternary spinodal decomposition and three-component liquid lens. Later, Kim [32] extended this idea to an arbitrary N-component ($N \geq 3$) CH fluid system and developed a generalized continuous surface tension formulation for incompressible multicomponent fluids. Using this multicomponent CH model, Lee and Kim [33] studied the dynamics of buoyancy-driven mixing in tilted channels via numerical simulations. Zhang et al. [34] proposed a geometric relation-based contact angle boundary condition for the ternary CH fluid model. By combining this with the immersed boundary method, Liu et al. [35] developed a modified ternary CH model to study the two-phase flow in complex domains. Li et al. [36] later developed a 3D version of the method by adopting a similar idea. For the stable simulation of the multicomponent CH model, Lee et al. [37] developed a temporally first-order accurate method based on the linear splitting scheme. Although a detailed stability analysis was not provided, the computational experiments showed the effectiveness of their proposed scheme despite the use of large time steps. Recently, Li et al. [38] constructed a temporally second-order accurate and unconditionally energy-stable scheme for the multicomponent CH systems. The energy dissipation law and unique solvability of the scheme were strictly proven.

It should be noted that the ternary and multicomponent CH models developed in [31,32] are the simplest combination of several binary CH equations. Although they can be successfully applied in various multiphase flow simulations, the effects of different surface tension coefficients were not considered. Boyer and Lapuerta [39] presented a three-component CH system that describes the effects of the surface tension and interactions between different components. Because the surface tension coefficients are equal, this ternary model and the model adopted in [31] are equivalent. Many researchers have constructed practical lattice Boltzmann algorithms to simulate ternary models in fluid systems [40–42]. However, it is difficult to prove the energy dissipation law using the lattice Boltzmann method. Based on the convex splitting method, Chen et al. [43] developed a nonlinear second-order time-accurate and energy-stable method for ternary CH equations [39]. To simplify the calculation and enhance the efficiency, Zhang and Yang [44] proposed a totally decoupled, linear, and unconditionally energy-stable time-marching scheme using the scalar auxiliary variable (SAV) technique. Owing to the coupling between the local and time-dependent auxiliary variables, decoupling the discrete system using the classical SAV approach increases the computational costs. To reduce the computation time and further simplify the algorithm, Yang and Kim [45] used a modified SAV method for ternary CH fluid models by following an idea similar to that in [25]. Despite the popularity of the SAV-type approaches in developing linear and energy-stable methods for phase-field systems, the resulting energy dissipation laws only hold with respect to a modified energy. In the discrete version, the relationship between the original and modified variable-based energies is unclear. To enhance the consistency of the classical SAV approach, Zhao [48] recently proposed a relaxation technique that satisfied the energy dissipation law, and significantly improved the consistency between the original and modified variable-based energies. For enhanced computational efficiency, Zhang and Shen [49] developed a variation of the SAV method with relaxation for general gradient flows.

Although SAV-type methods for ternary CH models were studied in [44,45], these only plotted the modified energy curves. The relationship between the original and modified energies were not investigated. More precisely, the modified energy stability could not analytically lead to the desired dissipation law with respect to the energy consisting of the original variables. If a relatively large time step is considered, then the difference between the original and modified energies may be significant. The present study aims to develop a novel time-marching method for ternary CH fluid models. By introducing novel time-dependent auxiliary variables including the free energy and kinetic energy, the proposed time-marching method has the following advantages: (i) The algorithm is efficient, and all variables can be updated in a step-by-step manner because of the linear and decoupled properties; (ii) The temporally second-order accuracy is satisfied based on the two-step backward differentiation formula (BDF2); (iii) The consistency between the original and modified energies is improved using a simple correction step; and (iv) The unique solvability of each variable can be analytically proved. To the best of the authors' knowledge, this is the first study focusing on linear, decoupled, and approximately original variable-based energy-stable methods for ternary CH systems coupled with incompressible fluid flows.

The remainder of this paper is organized as follows. In Section 2, the three-component CH model and its hydrodynamically coupled model are described. In Section 3, the time-marching schemes, energy relaxation techniques, and estimation of the unique solvability and energy dissipation properties are presented. Extensive computational tests are conducted in Section 4 to verify the proposed method. In Section 5, the potential applications to miscible liquid/liquid boundaries are discussed. The concluding remarks are presented in Section 6.

2. Original three-component models

2.1. Three-component CH model

The three-component CH system [39] can be deduced from the following free energy functional

$$E(\phi_1, \phi_2, \phi_3) = \frac{3\epsilon^2}{8} \sum_{k=1}^{3} \int_{\Omega} \Sigma_k |\nabla \phi_k|^2 \, d\mathbf{x} + 12 \int_{\Omega} F(\phi_1, \phi_2, \phi_3) \, d\mathbf{x}, \tag{1}$$

where Ω is the domain and $\mathbf{x}$ is the spatial variable. The concentration of each component is represented by $\phi_k = \phi_k(\mathbf{x}, t)$ ($k = 1, 2, 3$), where t is the temporal variable. We set $\phi_k = 1$ and 0 in the interior and exterior of k-th component, respectively. For each spatial position and time, the following conservative condition must be satisfied.

$$\phi_1(\mathbf{x}, t) + \phi_2(\mathbf{x}, t) + \phi_3(\mathbf{x}, t) = 1. \tag{2}$$

The linear gradient terms in Eq. (1) contribute to the mixing dynamics. The nonlinear term is defined as

$$F(\phi_1, \phi_2, \phi_3) = 3\Lambda \phi_1^2 \phi_2^2 \phi_3^2 + \sum_{k=1}^{3} \frac{\Sigma_k}{2} \phi_k^2 (1 - \phi_k^2), \tag{3}$$

which leads to phase separation. The thickness of the diffuse interface between the different components is related to a small positive constant ϵ; $\Lambda > 0$ is also a constant. The parameters Σ_k ($k = 1, 2, 3$) are defined as

$$\Sigma_1 = \sigma_{12} + \sigma_{13} - \sigma_{23}, \ \ \Sigma_2 = \sigma_{12} + \sigma_{23} - \sigma_{13}, \ \ \Sigma_3 = \sigma_{13} + \sigma_{23} - \sigma_{12}, \tag{4}$$

where σ_{mn} is the physical surface tension coefficient between the m-th and n-th components. From [39], the following well-posed condition should be satisfied

$$\Sigma_1 \Sigma_2 + \Sigma_1 \Sigma_3 + \Sigma_2 \Sigma_3 > 0, \ \text{and} \ \Sigma_m + \Sigma_n > 0, \ \text{for} \ m \neq n. \tag{5}$$

The authors in [39] proved the following two lemmas for a well-posed ternary CH model.

Lemma 1. *There exists $\overline{\Sigma}$ (≥ 0) that satisfies*

$$\Sigma_1 |\gamma_1|^2 + \Sigma_2 |\gamma_2|^2 + \Sigma_3 |\gamma_3|^2 \geq \overline{\Sigma}(|\gamma_1|^2 + |\gamma_2|^2 + |\gamma_3|^2), \ \text{for} \ \gamma_1 + \gamma_2 + \gamma_3 = 0,$$

if and only if the conditions (5) *hold.*

Lemma 2. *With a sufficiently large Λ, the nonlinear term $F(\phi_1, \phi_2, \phi_3)$ can be non-negative if the condition* (2) *holds.*

By taking the variational derivative of Eq. (1) with respect to ϕ_k and considering the condition (2), we derive the governing equations of a ternary CH system as follows:

$$\frac{\partial \phi_k}{\partial t} = \frac{M}{\Sigma_k} \Delta \mu_k, \tag{6}$$

$$\mu_k = -\frac{3\epsilon^2}{4} \Sigma_k \Delta \phi_k + 12(f_k + \beta), \ \text{for} \ k = 1, 2, 3, \tag{7}$$

where M is the positive mobility and f_k is the derivative of $F(\phi_1, \phi_2, \phi_3)$ with respect to ϕ_k. To ensure that condition (2) holds, we define $\beta = -\Sigma_T \sum_{k=1}^{3}(f_k/\Sigma_k)$ and $1/\Sigma_T = \sum_{k=1}^{3}(1/\Sigma_k)$ [39,44,45]. A periodic or zero Neumann boundary condition is considered.

$$\nabla \phi_k \cdot \mathbf{n}|_{\partial \Omega} = 0, \ \ \nabla \mu_k \cdot \mathbf{n}|_{\partial \Omega} = 0, \ \text{for} \ k = 1, 2, 3.$$

From Eq. (7) and condition (2), we derive $\sum_{k=1}^{3} \mu_k / \Sigma_k = 0$. Then, we recast Eqs. (6) and (7) to be the following equivalent forms:

$$\frac{\partial \phi_k}{\partial t} = \frac{M}{\Sigma_k} \Delta \mu_k, \tag{8}$$

$$\mu_k = -\frac{3\epsilon^2}{4} \Sigma_k \Delta \phi_k + 12(f_k + \beta), \ \text{for} \ k = 1, 2, \tag{9}$$

$$\phi_3 = 1 - \phi_1 - \phi_2, \ \ \mu_3 = -\Sigma_3 \left(\frac{\mu_1}{\Sigma_1} + \frac{\mu_2}{\Sigma_2} \right). \tag{10}$$

The detailed proof of equivalence is provided in [44]. A comparison with Eqs. (6) and (7) shows that Eqs. (8)–(10) are more efficient because only ϕ_1 and ϕ_2 need to be calculated at each time step, and ϕ_3 can be directly updated.

For two functions $q_1 = q_1(\mathbf{x})$ and $q_2 = q_2(\mathbf{x})$, their L^2-inner product is defined as $(q_1, q_2) = \int_\Omega q_1 q_2 \, d\mathbf{x}$. The corresponding L^2-norm is defined as $\|q_1\|^2 = (q_1, q_1)$. With the definitions of the L^2-inner products and L^2-norm, we take the L^2-inner product of Eq. (6) with $-\mu_k$, and of Eq. (7) with $\partial \phi_k / \partial t$. By applying the integrations by parts and the appropriate boundary conditions (periodic or zero Neumann), and then combining the results for $k = 1, 2, 3$, the following energy dissipation law is obtained.

$$\frac{d}{dt} E(\phi_1, \phi_2, \phi_3) = -M \sum_{k=1}^{3} \left(\Sigma_k \| \nabla \frac{\mu_k}{\Sigma_k} \|^2 \right) \leq -M\overline{\Sigma} \sum_{k=1}^{3} \left(\| \nabla \frac{\mu_k}{\Sigma_k} \|^2 \right) \leq 0. \tag{11}$$

The above inequality shows that the ternary CH system dissipates the free energy over time.

2.2. Three-component CH model with incompressible fluids

By adding the convection term into Eq. (6) and coupling the incompressible Navier–Stokes (NS) equations, a dimensionless version of the incompressible three-component CH fluid model can be expressed as

$$\frac{\partial \mathbf{u}}{\partial t} + \mathbf{u} \cdot \nabla \mathbf{u} = -\nabla p + \frac{1}{Re} \Delta \mathbf{u} - \sum_{k=1}^{3} \phi_k \nabla \mu_k, \tag{12}$$

$$\nabla \cdot \mathbf{u} = 0, \tag{13}$$

$$\frac{\partial \phi_k}{\partial t} + \nabla \cdot (\phi_k \mathbf{u}) = M \Delta \frac{\mu_k}{\Sigma_k}, \tag{14}$$

$$\mu_k = -\frac{3\epsilon^2}{4} \Sigma_k \Delta c_k + 12(f_k + \beta), \ \text{for} \ k = 1, 2, 3, \tag{15}$$

where $\mathbf{u}$ is the velocity field. In two-dimensional (2D) and 3D spaces, $\mathbf{u} = (u, v)$ and $\mathbf{u} = (u, v, w)$, respectively. Here, u, v, and w are the velocity components along the x-, y-, and z-directions, respectively; and p is the pressure. The last term in Eq. (12) is the effect of surface tension [47]. The incompressible condition is expressed by Eq. (13). $Re > 0$ is related to the viscosity of fluid. For all variables, the periodic or following boundary conditions are considered.

$$\mathbf{u}|_{\partial\Omega} = 0, \ \nabla p \cdot \mathbf{n}|_{\partial\Omega} = 0, \ \nabla\phi_k \cdot \mathbf{n}|_{\partial\Omega} = 0, \ \nabla\mu_k \cdot \mathbf{n}|_{\partial\Omega} = 0, \ \text{for } k = 1, 2, 3.$$

To reduce the computational time, the governing equations are transformed into the following equivalent forms:

$$\frac{\partial \mathbf{u}}{\partial t} + \mathbf{u} \cdot \nabla \mathbf{u} = -\nabla p + \frac{1}{Re}\Delta\mathbf{u} - \sum_{k=1}^{3} \phi_k \nabla\mu_k, \tag{16}$$

$$\nabla \cdot \mathbf{u} = 0, \tag{17}$$

$$\frac{\partial\phi_k}{\partial t} + \nabla \cdot (\phi_k\mathbf{u}) = M\Delta\frac{\mu_k}{\Sigma_k}, \tag{18}$$

$$\mu_k = -\frac{3\epsilon^2}{4}\Sigma_k\Delta\phi_k + 12(f_k + \beta), \ \text{for } k = 1, 2, \tag{19}$$

$$\phi_3 = 1 - \phi_1 - \phi_2, \ \mu_3 = -\Sigma_3\left(\frac{\mu_1}{\Sigma_1} + \frac{\mu_2}{\Sigma_2}\right). \tag{20}$$

By taking the L^2-inner products of Eq. (12) with $\mathbf{u}$, of Eq. (14) with $-\mu_k$, and of Eq. (15) with $\partial\phi_k/\partial t$; using the integration by parts and appropriate boundary conditions, and then combining the results for $k = 1, 2, 3$, the following energy dissipation law is derived.

$$\frac{d}{dt}E(\mathbf{u}, \phi_1, \phi_2, \phi_3) = -\frac{1}{Re}\|\nabla\mathbf{u}\|^2 - M\sum_{k=1}^{3}\Sigma_k\|\frac{\nabla\mu_k}{\Sigma_k}\|^2 \leq -\frac{1}{Re}\|\nabla\mathbf{u}\|^2$$

$$-\overline{\Sigma}M\sum_{k=1}^{3}\|\frac{\nabla\mu_k}{\Sigma_k}\|^2 \leq 0. \tag{21}$$

The total energy functional is defined as

$$E(\mathbf{u}, \phi_1, \phi_2, \phi_3) = \int_\Omega \frac{1}{2}|\mathbf{u}|^2 \, \mathbf{x} + \int_\Omega \left(\frac{3\epsilon^2}{8}\sum_{k=1}^{3}\Sigma_k|\nabla\phi_k|^2 + 12F(\phi_1, \phi_2, \phi_3)\right) d\mathbf{x}, \tag{22}$$

where the first and second integral terms correspond to the kinetic energy of the NS equations and the free energy of ternary CH model, respectively. The above inequality indicates that the incompressible three-component CH fluid system dissipates the total energy over time.

3. Numerical methods, analysis, and implementations

In this section, we construct temporally second-order, linearly implicit-explicit, and energy-stable schemes for ternary CH fluid models using a variation of the SAV technique. From [39], we know that Lemma 1, Lemma 2, and condition (2) ensure that the free energy of the ternary CH model is bounded from below. Two time-dependent auxiliary variables are defined as follows

$$R = R(t) = E(\phi_1, \phi_2, \phi_3) + B_1, \tag{23}$$

$$Q = Q(t) = E(\mathbf{u}, \phi_1, \phi_2, \phi_3) + B_2, \tag{24}$$

where $E(\phi_1, \phi_2, \phi_3)$ and $E(\mathbf{u}, \phi_1, \phi_2, \phi_3)$ are the energy functionals defined by Eqs. (1) and (22), respectively. The positive constants B_1 and B_2 are used to ensure that $R > 0$ and $Q > 0$. Let $r = R - B_1$ and $q = Q - B_2$, it is observed that $r = E(\phi_1, \phi_2, \phi_3)$ and $q = E(\mathbf{u}, \phi_1, \phi_2, \phi_3)$.

3.1. Numerical scheme for the ternary CH model

We define $U = R/(E(\phi_1, \phi_2, \phi_3) + B_1)$ and $V = U(2 - U)$. In the continuous version, $U = 1$ and $V = 1$ hold true. Equations (6) and (7) can be recast as

$$\frac{\partial\phi_k}{\partial t} = \frac{M}{\Sigma_k}\Delta\mu_k, \tag{25}$$

$$\mu_k = \frac{3\epsilon^2}{4}\Sigma_k\Delta\phi_k + 12(f_k + \beta)V, \tag{26}$$

$$V = U(2 - U), \tag{27}$$

$$U = \frac{R}{E(\phi_1, \phi_2, \phi_3) + B_1}, \tag{28}$$

$$\frac{dR}{dt} = -\frac{R}{E(\phi_1, \phi_2, \phi_3) + B_1}M\sum_{k=1}^{3}\left(\Sigma_k\|\nabla\frac{\mu_k}{\Sigma_k}\|^2\right), \ \text{for } k = 1, 2, 3. \tag{29}$$

Because $R/(E(\phi_1, \phi_2, \phi_3) + B_1) = 1$, R equals to the summation of the free energy and a constant, and the energy dissipation law in Eq. (11) leads to Eq. (29). We find that Eqs. (25) and (26) are equivalent to Eqs. (6) and (7) because $V = 1$ in continuous version. Based on Eqs. (25)–(29), the linear and second-order time-accurate method is constructed as

$$\frac{3\phi_k^{n+1} - 4\phi_k^n + \phi_k^{n-1}}{2\Delta t} = M\Delta\frac{\mu_k^{n+1}}{\Sigma_k}, \tag{30}$$

$$\mu_k^{n+1} = -\frac{3\epsilon^2}{4}\Sigma_k\Delta\phi_k^{n+1} + 12(f_k^* + \beta^*)V^{n+1} + S\Sigma_k(\phi_k^{n+1} - \phi_k^*), \tag{31}$$

$$V^{n+1} = U^{n+1}(2 - U^{n+1}), \tag{32}$$

$$U^{n+1} = \frac{R^{n+1}}{E(\phi_1^*, \phi_2^*, \phi_3^*) + B_1}, \tag{33}$$

$$\frac{R^{n+1} - R^n}{\Delta t} = -\frac{R^{n+1}}{E(\phi_1^*, \phi_2^*, \phi_3^*) + B_1}M\sum_{k=1}^{3}\left(\Sigma_k\|\nabla\frac{\mu_k^*}{\Sigma_k}\|^2\right), \text{ for } k = 1, 2, 3, \tag{34}$$

where Δt is the uniform time step, ϕ^{n+1} is the approximation of $\phi((n+1)\Delta t)$, and $\phi^* = 2\phi^n - \phi^{n-1}$ is the linear extrapolation. To develop linear and totally decoupled scheme, all nonlinear terms are explicitly treated. For enhanced stability, the stabilization term (last term) in Eq. (31) is adopted. We consider the periodic or zero Neumann boundary conditions:

$$\nabla\phi_k^{n+1} \cdot \mathbf{n}|_{\partial\Omega} = 0, \quad \nabla\mu_k^{n+1} \cdot \mathbf{n}|_{\partial\Omega} = 0, \text{ for } k = 1, 2, 3.$$

To reduce computational costs, Eqs. (30)–(34) can be recast as

$$\frac{3\phi_k^{n+1} - 4\phi_k^n + \phi_k^{n-1}}{2\Delta t} = M\Delta\frac{\mu_k^{n+1}}{\Sigma_k}, \tag{35}$$

$$\mu_k^{n+1} = -\frac{3\epsilon^2}{4}\Sigma_k\Delta\phi_k^{n+1} + 12(f_k^* + \beta^*)V^{n+1} + S\Sigma_k(\phi_k^{n+1} - \phi_k^*), \tag{36}$$

$$V^{n+1} = U^{n+1}(2 - U^{n+1}), \tag{37}$$

$$U^{n+1} = \frac{R^{n+1}}{E(\phi_1^*, \phi_2^*, \phi_3^*) + B_1}, \tag{38}$$

$$\frac{R^{n+1} - R^n}{\Delta t} = -\frac{R^{n+1}}{E(\phi_1^*, \phi_2^*, \phi_3^*) + B_1}M\sum_{k=1}^{3}\left(\Sigma_k\|\nabla\frac{\mu_k^*}{\Sigma_k}\|^2\right), \text{ for } k = 1, 2 \tag{39}$$

$$\phi_3^{n+1} = 1 - \phi_1^{n+1} - \phi_2^{n+1}, \quad \mu_3^{n+1} = -\Sigma_3\left(\frac{\mu_1^{n+1}}{\Sigma_1} + \frac{\mu_2^{n+1}}{\Sigma_2}\right). \tag{40}$$

Here, the conditions $\sum_{k=1}^{3}\phi_k = 1$ and $\sum_{k=1}^{3}\mu_k/\Sigma_k = 0$ are used. In fact, Eq. (39) is a temporally first-order scheme, i.e., $R^{n+1} = R(t^{n+1}) + O(\Delta t)$. Thus, we get

$$U^{n+1} = U(t^{n+1}) + C\Delta t = 1 + C\Delta t,$$

where C is a constant that is independent of Δt. We can derive

$$V^{n+1} = U^{n+1}(2 - U^{n+1}) = (1 + C\Delta t)(1 - C\Delta t) = 1 - C^2\Delta t^2.$$

It can be observed that V^{n+1} is a temporally second-order numerical solution of 1. This implies that V^{n+1} does not affect the second-order accuracy of Eqs. (35) and (36).

Theorem 3.1. *With the previous information, Eqs. (35)–(40) have unique solutions R^{n+1} and ϕ_k^{n+1} for $k = 1, 2, 3$.*

Proof. First, we recast Eq. (39) as

$$R^{n+1} = \frac{R^n}{1 + \Delta t M\sum_{k=1}^{3}\left(\Sigma_k\|\nabla\frac{\mu_k^*}{\Sigma_k}\|^2\right)/(E(\phi_1^*, \phi_2^*, \phi_3^*) + B_1)}. \tag{41}$$

The non-negativity of $(E(\phi_1^*, \phi_2^*, \phi_3^*) + B_1)$ is straightforward. Furthermore, we have

$$\sum_{k=1}^{3}\left(\Sigma_k\|\nabla\frac{\mu_k^*}{\Sigma_k}\|^2\right) \geq \overline{\Sigma}\sum_{k=1}^{3}\left(\|\nabla\frac{\mu_k^*}{\Sigma_k}\|^2\right) > 0.$$

The denominator of Eq. (41) is larger than zero. Therefore, the unique solvability of R^{n+1} is proved. With the computed R^{n+1}, U^{n+1} and V^{n+1} can be directly updated from Eqs. (38) and (37), successively. By substituting μ_k^{n+1} in Eq. (35) with Eq. (36), we get

$$\frac{3\phi_k^{n+1} - 4\phi_k^n + \phi_k^{n-1}}{2\Delta t} = -\frac{3M\epsilon^2}{4}\Delta^2\phi_k^{n+1} + \frac{12MV^{n+1}}{\Sigma_k}\Delta(f_k^* + \beta^*)$$
$$+ SM\Delta(\phi_k^{n+1} - \phi_k^*). \tag{42}$$

Here, $k = 1, 2, 3$. Now, we estimate the unique solvability of the above equation. We introduce the following convex functional

$$\mathcal{G}(\phi_k) = \int_\Omega \left[\frac{3}{4\Delta t}|\phi_k|^2 + \frac{SM}{2}|\nabla\phi_k|^2 + \frac{3M\epsilon^2}{8}|\Delta\phi_k|^2 + g^{n,n-1}\phi_k\right]d\mathbf{x}, \tag{43}$$

where

$$g^{n,n-1} = \frac{-4\phi_k^n + \phi_k^{n-1}}{2\Delta t} - \frac{12MV^{n+1}}{\Sigma_k}\Delta(f_k^* + \beta^*) + SM\Delta\phi_k^*.$$

By applying the variational derivative of $\mathcal{G}(\phi_k)$ with respect to ϕ_k^{n+1}, we have

$$\left.\frac{\vartheta\mathcal{G}}{\vartheta\phi_k}\right|_{\phi_k = \phi_k^{n+1}} = \frac{3}{2\Delta t}\phi_k^{n+1} - SM\Delta\phi_k^{n+1} + \frac{3M\epsilon^2}{4}\Delta^2\phi_k^{n+1} + g^{n,n-1}, \tag{44}$$

where ϑ is the variational operator. Because $\vartheta\mathcal{G}/\vartheta\phi_k = 0$, the minimum value of a convex functional $\mathcal{G}(\phi_k)$ uniquely exists. In this sense, the minimization of $\mathcal{G}(\phi_k)$ is equivalent to obtaining ϕ_k^{n+1} from Eq. (42). Thus, the unique solvability is proved. $\square$

Theorem 3.2. *The numerical solutions of Eqs.* (35)–(40) *unconditionally dissipate the time-discretized modified energy.*

Proof. With the initial condition $R^0 > 0$, we conclude that the computed R^1 from Eq. (41) is non-negative because the denominator of Eq. (41) is positive. It is evident that $R^{n+1} \geq 0$ holds by the induction. From Eq. (39), the following inequality can be derived

$$R^{n+1} - R^n = -\Delta t M \sum_{k=1}^3 \left(\Sigma_k \|\nabla\frac{\mu_k^*}{\Sigma_k}\|^2\right)\frac{R^{n+1}}{(E(\phi_1^*, \phi_2^*, \phi_3^*) + B_1)}$$
$$\leq -\Delta t M \overline{\Sigma} \sum_{k=1}^3 \left(\|\nabla\frac{\mu_k^*}{\Sigma_k}\|^2\right)\frac{R^{n+1}}{(E(\phi_1^*, \phi_2^*, \phi_3^*) + B_1)} \leq 0. \tag{45}$$

Let $\hat{r}^{n+1} = R^{n+1} - B_1$, then the above inequality indicates that $\hat{r}^{n+1} \leq \hat{r}^n$ holds. Here, $\hat{r}^{n+1}$ is a modified version of the energy. Thus the time-discretized modified energy dissipation law is proved. $\square$

Energy relaxation technique. From Theorem 3.2, we conclude that the numerical solutions unconditionally dissipate the modified energy r^{n+1}. Although the modified energy r equals to the original energy $E(\phi_1, \phi_2, \phi_3)$ in a continuous version, there is no constraint to ensure that the numerical solution of $\hat{r}^{n+1}$ equals to $E(\phi_1^{n+1}, \phi_2^{n+1}, \phi_3^{n+1})$ in the time-discretized version. The difference between $\hat{r}^{n+1}$ and $E(\phi_1^{n+1}, \phi_2^{n+1}, \phi_3^{n+1})$ may become more obvious when the time step is increased. This indicates that the computed modified energy $\hat{r}^{n+1}$ is not the desired original variable-based energy. To resolve this problem, we refer to the idea of [49] and present the following energy relaxation step

$$R_o^{n+1} = \xi_0 R^{n+1} + (1 - \xi_0)(E(\phi_1^{n+1}, \phi_2^{n+1}, \phi_2^{n+1}) + B_1),\ \xi_0 \in \chi, \tag{46}$$

where

$$\chi = \left\{\xi_0 \in [0, 1]\ s.t.\ \frac{R_o^{n+1} - R^{n+1}}{\Delta t} \leq -\theta^{n+1}\Psi^{n+1} + \frac{R^{n+1}}{E(\phi_1^*, \phi_2^*, \phi_3^*) + B_1}\Psi^*\right\}, \tag{47}$$

and $\Psi = M\sum_{k=1}^3\left(\Sigma_k\|\nabla\frac{\mu_k}{\Sigma_k}\|^2\right)$. As $\xi = 1$ belongs to χ, χ is not empty. θ^{n+1} is non-negative and will be determined. By substituting R_o^{n+1} in Eq. (47) with Eq. (46), we obtain the following inequality

$$(R^{n+1} - (E(\phi_1^{n+1}, \phi_2^{n+1}, \phi_3^{n+1}) + B_1))\xi_0 \leq R^{n+1} - (E(\phi_1^{n+1}, \phi_2^{n+1}, \phi_3^{n+1}) + B_1)$$
$$-\Delta t\theta^{n+1}\Psi^{n+1} + \Delta t\frac{R^{n+1}}{(E(\phi_1^*, \phi_2^*, \phi_3^*) + B_1)}\Psi^*. \tag{48}$$

The selection of ξ_0 and θ^{n+1} is described by the following theorem.

Theorem 3.3. *The possible choices of ξ_0 and θ^{n+1} are given as follows:*

Case 1. If $R^{n+1} = (E(\phi_1^{n+1}, \phi_2^{n+1}, \phi_3^{n+1}) + B_1)$, then let $\xi_0 = 0$ and $\theta^{n+1} = \frac{R^{n+1}\Psi^*}{(E(\phi_1^*, \phi_2^*, \phi_3^*) + B_1)\Psi^{n+1}}$;

Case 2. If $R^{n+1} > (E(\phi_1^{n+1}, \phi_2^{n+1}, \phi_3^{n+1}) + B_1)$, then let $\xi_0 = 0$ and

$$\theta^{n+1} = \frac{R^{n+1} - (E(\phi_1^{n+1}, \phi_2^{n+1}, \phi_3^{n+1}) + B_1)}{\Delta t \Psi^{n+1}} + \frac{R^{n+1}\Psi^*}{(E(\phi_1^*, \phi_2^*, \phi_3^*) + B_1)\Psi^{n+1}};$$

Case 3. If $R^{n+1} < (E(\phi_1^{n+1}, \phi_2^{n+1}, \phi_3^{n+1}) + B_1)$ and $R^{n+1} - (E(\phi_1^{n+1}, \phi_2^{n+1}, \phi_3^{n+1}) + B_1) + \Delta t \frac{R^{n+1}}{(E(\phi_1^*, \phi_2^*, \phi_3^*) + B_1)}\Psi^* \geq 0$, then let $\xi_0 = 0$ and

$$\theta^{n+1} = \frac{R^{n+1} - (E(\phi_1^{n+1}, \phi_2^{n+1}, \phi_3^{n+1}) + B_1)}{\Delta t \Psi^{n+1}} + \frac{R^{n+1}\Psi^*}{(E(\phi_1^*, \phi_2^*, \phi_3^*) + B_1)\Psi^{n+1}};$$

Case 4. If $R^{n+1} < (E(\phi_1^{n+1}, \phi_2^{n+1}, \phi_3^{n+1}) + B_1)$ and $R^{n+1} - (E(\phi_1^{n+1}, \phi_2^{n+1}, \phi_3^{n+1}) + B_1) + \Delta t \frac{R^{n+1}}{(E(\phi_1^*, \phi_2^*, \phi_3^*) + B_1)}\Psi^* < 0$, we let $\theta^{n+1} = 0$ and

$$\xi_0 = 1 - \frac{\Delta t R^{n+1} \Psi^*}{(E(\phi_1^*, \phi_2^*, \phi_3^*) + B_1)(E(\phi_1^{n+1}, \phi_2^{n+1}, \phi_3^{n+1}) + B_1 - R^{n+1})}.$$

For Cases 1–4, $\xi_0 \in \chi$ and inequality (48) holds. When $R_o^n \geq 0$ and $R_0^{n+1} \geq 0$, the following inequality is satisfied

$$R_o^{n+1} - R_o^n \leq -\Delta t \theta^{n+1} \Psi^{n+1} \leq 0, \tag{49}$$

which indicates that the corrected energy (i.e., R_o^{n+1}) still satisfies the dissipation law. Moreover, $R^{n+1} \leq (E(\phi_1^{n+1}, \phi_2^{n+1}, \phi_3^{n+1}) + B_1)$.

Proof. With ξ_0 and θ^{n+1} defined in all four cases, we have $\xi_0 \in \chi$, i.e., $\xi_0 \in [0, 1]$. As mentioned in Theorem 3.2, $R^{n+1} \geq 0$ holds true. Moreover, $E(\phi_1^{n+1}, \phi_2^{n+1}, \phi_3^{n+1}) + B_1 \geq 0$ also holds. From Eq. (46), we have $R_o^{n+1} \geq 0$. By combining equalities (39) and (47), we obtain inequality (49). In Cases 1–3, we have $R_o^{n+1} = (E(\phi_1^{n+1}, \phi_2^{n+1}, \phi_3^{n+1}) + B_1)$ because $\xi_0 = 0$. In Case 4, because $R^{n+1} \leq (E(\phi_1^{n+1}, \phi_2^{n+1}, \phi_3^{n+1}) + B_1)$ and $\xi_0 \in [0, 1]$ are known, $R_o^{n+1} \leq (E(\phi_1^{n+1}, \phi_2^{n+1}, \phi_3^{n+1}) + B_1)$ can be derived from Eq. (46). Thus, the proof is completed. $\square$

In each time iteration, the numerical implementation is summarized as follows:

Step 1. Compute R^{n+1} using Eq. (41);
Step 2. Update U^{n+1} and V^{n+1} from Eqs. (38) and (37), respectively;
Step 3. Calculate ϕ_k^{n+1} and μ_k^{n+1} ($k = 1, 2$) from Eqs. (35) and (36), respectively;
Step 4. Update ϕ_3^{n+1} and μ_3^{n+1} using Eq. (40);
Step 5. Update R_o^{n+1} using Eq. (46);
Step 6. Replace R^{n+1} with R_o^{n+1} and then enter the next time step.

Remark 3.1. By defining the relaxed energy as $r^{n+1} = R_o^{n+1} - B_1$, we can verify that r^{n+1} is bounded from below because $R_o^{n+1} \geq 0$. Furthermore, we find that r^{n+1} equals to the time-discretized original energy $E(\phi_1^{n+1}, \phi_2^{n+1}, \phi_3^{n+1})$ in most cases (Cases 1–3). Therefore, the energy dissipation law with respect to the relaxed energy r^{n+1} is equivalent to that with respect to the original variable energy $E(\phi_1^{n+1}, \phi_2^{n+1}, \phi_3^{n+1})$. In Case 4, the relaxed energy r^{n+1} is an approximation of $E(\phi_1^{n+1}, \phi_2^{n+1}, \phi_3^{n+1})$, and is located in $(\hat{r}^{n+1}, E(\phi_1^{n+1}, \phi_2^{n+1}, \phi_3^{n+1}))$, where $\hat{r}^{n+1}$ is the modified energy defined above. Therefore, the energy relaxation technique leads to the appropriate dissipation law based on original variables.

3.2. Numerical scheme for the ternary fluid model

Let $U = R/(E(\mathbf{u}, \phi_1, \phi_2, \phi_3) + B_2)$ and $V = U(2 - U)$. In the time-continuous version, $U = V = 1$. The original ternary CH fluid system (12)–(15) is recast as

$$\frac{\partial \mathbf{u}}{\partial t} + V\mathbf{u} \cdot \nabla \mathbf{u} = -\nabla p + \frac{1}{Re}\Delta \mathbf{u} - V \sum_{k=1}^{3} \phi_k \nabla \mu_k, \tag{50}$$

$$\nabla \cdot \mathbf{u} = 0, \tag{51}$$

$$\frac{\partial \phi_k}{\partial t} + V\nabla \cdot (\phi_k \mathbf{u}) = M\Delta \frac{\mu_k}{\Sigma_k}, \tag{52}$$

$$\mu_k = -\frac{3\epsilon^2}{4}\Sigma_k \Delta \phi_k + 12(f_k + \beta)V, \tag{53}$$

$$V = U(2 - U), \tag{54}$$

$$U = \frac{R}{E(\mathbf{u}, \phi_1, \phi_2, \phi_3) + B_2}, \tag{55}$$

$$\frac{\partial R}{\partial t} = -\left(\frac{R}{E(\mathbf{u}, \phi_1, \phi_2, \phi_3) + B_2}\right)\left[\frac{1}{Re}\|\nabla \mathbf{u}\|^2 + M \sum_{k=1}^{3}\Sigma_k\|\frac{\nabla \mu_k}{\Sigma_k}\|^2\right], \text{ for } k = 1, 2, 3. \tag{56}$$

The linearly implicit-explicit, second-order time-accurate scheme is constructed as

$$\frac{3\tilde{\mathbf{u}}^{n+1} - 4\mathbf{u}^n + \mathbf{u}^{n-1}}{2\Delta t} + V^{n+1}\mathbf{u}^* \cdot \nabla \mathbf{u}^* = -\nabla p^n + \frac{1}{Re}\Delta\tilde{\mathbf{u}}^{n+1} - V^{n+1}\sum_{k=1}^{3}\phi_k^*\nabla\mu_k^*, \tag{57}$$

$$\frac{3\mathbf{u}^{n+1} - 3\tilde{\mathbf{u}}^{n+1}}{2\Delta t} = -\nabla(p^{n+1} - p^n), \tag{58}$$

$$\nabla \cdot \mathbf{u}^{n+1} = 0, \tag{59}$$

$$\frac{3\phi_k^{n+1} - 4\phi_k^n + \phi_k^{n-1}}{2\Delta t} + V^{n+1}\nabla \cdot (\mathbf{u}^*\phi_k^*) = M\Delta\frac{\mu_k^{n+1}}{\Sigma_k}, \tag{60}$$

$$\mu_k^{n+1} = -\frac{3\epsilon^2}{4}\Sigma_k\Delta\phi_k^{n+1} + 12(f_k^* + \beta^*)V^{n+1} + S\Sigma_k(\phi_k^{n+1} - \phi_k^*), \tag{61}$$

$$V^{n+1} = U^{n+1}(2 - U^{n+1}), \tag{62}$$

$$U^{n+1} = \frac{R^{n+1}}{E(\mathbf{u}^*, \phi_1^*, \phi_2^*, \phi_3^*) + B_2}, \tag{63}$$

$$\frac{R^{n+1} - R^n}{\Delta t} = -\left(\frac{R^{n+1}}{E(\mathbf{u}^*, \phi_1^*, \phi_2^*, \phi_3^*) + B_2}\right)\left[\frac{1}{Re}\|\nabla\mathbf{u}^*\|^2 + M\sum_{k=1}^{3}\Sigma_k\|\frac{\nabla\mu_k^*}{\Sigma_k}\|^2\right],$$
$$\text{for } k = 1, 2, 3, \tag{64}$$

where a projection method is used to treat the momentum equation and $\tilde{\mathbf{u}}^{n+1}$ is the intermediate velocity. We consider the periodic or following time-discretized boundary conditions:

$$\mathbf{u}^{n+1} \cdot \mathbf{n}|_{\partial\Omega} = 0, \ \tilde{\mathbf{u}}^{n+1}|_{\partial\Omega} = 0, \ \nabla p^{n+1} \cdot \mathbf{n}|_{\partial\Omega} = 0,$$
$$\nabla c_k^{n+1} \cdot \mathbf{n}|_{\partial\Omega} = 0, \ \nabla\mu_k^{n+1} \cdot \mathbf{n}|_{\partial\Omega} = 0, \ \text{for } k = 1, 2, 3.$$

For an efficient computation, we simplify the governing equations as

$$\frac{3\tilde{\mathbf{u}}^{n+1} - 4\mathbf{u}^n + \mathbf{u}^{n-1}}{2\Delta t} + V^{n+1}\mathbf{u}^* \cdot \nabla\mathbf{u}^* = -\nabla p^n + \frac{1}{Re}\Delta\tilde{\mathbf{u}}^{n+1} - V^{n+1}\sum_{k=1}^{3}\phi_k^*\nabla\mu_k^*, \tag{65}$$

$$\frac{3\mathbf{u}^{n+1} - 3\tilde{\mathbf{u}}^{n+1}}{2\Delta t} = -\nabla(p^{n+1} - p^n), \tag{66}$$

$$\nabla \cdot \mathbf{u}^{n+1} = 0, \tag{67}$$

$$\frac{3\phi_k^{n+1} - 4\phi_k^n + \phi_k^{n-1}}{2\Delta t} + V^{n+1}\nabla \cdot (\mathbf{u}^*\phi_k^*) = M\Delta\frac{\mu_k^{n+1}}{\Sigma_k}, \tag{68}$$

$$\mu_k^{n+1} = -\frac{3\epsilon^2}{4}\Sigma_k\Delta\phi_k^{n+1} + 12(f_k^* + \beta^*)V^{n+1} + S\Sigma_k(\phi_k^{n+1} - \phi_k^*), \ \text{for } k = 1, 2, \tag{69}$$

$$V^{n+1} = U^{n+1}(2 - U^{n+1}), \tag{70}$$

$$U^{n+1} = \frac{R^{n+1}}{E(\mathbf{u}^*, \phi_1^*, \phi_2^*, \phi_3^*) + B_2}, \tag{71}$$

$$\frac{R^{n+1} - R^n}{\Delta t} = -\left(\frac{R^{n+1}}{E(\mathbf{u}^*, \phi_1^*, \phi_2^*, \phi_3^*) + B_2}\right)\left[\frac{1}{Re}\|\nabla\mathbf{u}^*\|^2 + M\sum_{k=1}^{3}\Sigma_k\|\frac{\nabla\mu_k^*}{\Sigma_k}\|^2\right], \tag{72}$$

$$\phi_3^{n+1} = 1 - \phi_1^{n+1} - \phi_2^{n+1}, \ \mu_3^{n+1} = -\Sigma_3\left(\frac{\mu_1^{n+1}}{\Sigma_1} + \frac{\mu_2^{n+1}}{\Sigma_2}\right). \tag{73}$$

Because V^{n+1} is a second-order approximation of 1, the second-order accuracy of Eqs. (65)–(69) is not affected.

Theorem 3.4. *With previous information, Eqs. (65)–(73) have unique solutions R^{n+1}, ϕ_k^{n+1} for $k = 1, 2, 3$, $\mathbf{u}^{n+1}$, and p^{n+1}.*

Proof. First, we reformulate Eq. (39) as

$$R^{n+1} = \frac{R^n}{1 + \Delta t\left[\frac{1}{Re}\|\nabla\mathbf{u}^*\|^2 + M\sum_{k=1}^{3}\left(\Sigma_k\|\nabla\frac{\mu_k^*}{\Sigma_k}\|^2\right)\right]\bigg/(E(\mathbf{u}, \phi_1^*, \phi_2^*, \phi_3^*) + B_2)}. \tag{74}$$

From the previous analysis, we find that the denominator of Eq. (74) is greater than zero. The unique solvability of R^{n+1} is straightforward. Next, U^{n+1} and V^{n+1} are directly updated from Eqs. (71) and (70), respectively. To validate the unique solvability of c_k^{n+1}, we combine Eqs. (68) and (69) and obtain

$$\frac{3\phi_k^{n+1} - 4\phi_k^n + \phi_k^{n-1}}{2\Delta t} + V^{n+1}\nabla\cdot(\mathbf{u}^*\phi_k^*) = -\frac{3M\epsilon^2}{4}\Delta^2\phi_k^{n+1} + \frac{12MV^{n+1}}{\Sigma_k}\Delta(f_k^* + \beta^*)$$
$$+ SM\Delta(\phi_k^{n+1} - \phi_k^*). \tag{75}$$

We introduce the following convex functional

$$\mathcal{Q}(\phi_k) = \int_\Omega \left[\frac{3}{4\Delta t}|\phi_k|^2 + \frac{SM}{2}|\nabla\phi_k|^2 + \frac{3M\epsilon^2}{8}|\Delta\phi_k|^2 + q^{n,n-1}\phi_k \right] d\mathbf{x}, \tag{76}$$

where

$$q^{n,n-1} = \frac{-4\phi_k^n + \phi_k^{n-1}}{2\Delta t} + V^{n+1}\nabla\cdot(\mathbf{u}^*\phi_k^*) - \frac{12MV^{n+1}}{\Sigma_k}\Delta(f_k^* + \beta^*) + SM\Delta\phi_k^*.$$

By applying the variational derivative of $\mathcal{Q}(\phi_k)$ with respect to ϕ_k^{n+1}, we obtain

$$\frac{\vartheta\mathcal{Q}}{\vartheta\phi_k}\bigg|_{\phi_k=\phi_k^{n+1}} = \frac{3}{2\Delta t}\phi_k^{n+1} - SM\Delta\phi_k^{n+1} + \frac{3M\epsilon^2}{4}\Delta^2\phi_k^{n+1} + q^{n,n-1}. \tag{77}$$

Because $\vartheta\mathcal{Q}/\vartheta\phi_k = 0$, the minimum value of the convex functional $\mathcal{Q}(c_k)$ exists uniquely. Therefore, the minimization of $\mathcal{Q}(\phi_k)$ is equivalent to obtaining ϕ_k^{n+1} from Eq. (75). The unique solvability of Eqs. (68) and (69) is proved. For ϕ^{n+1}, it is explicitly updated from Eq. (73). The unique solvability of Eq. (65) is easily proved by the processes mentioned above. We herein omit these similar steps and recommend that interested readers refer to [45,46] for more details. With computed $\tilde{\mathbf{u}}^{n+1}$, we can update p^{n+1} by solving a Poisson equation derived by applying the divergence operator to Eq. (66) and adopting Eq. (67). In general, the Poisson equation with zero Neumann or periodic boundary conditions does not have a unique solution. However, the unique solution can be defined by forcing the summation of the solution to be zero [50]. With the computed p^{n+1} and $\tilde{\mathbf{u}}^{n+1}$, we can update $\mathbf{u}^{n+1}$ using Eq. (66). The proof of the unique solvability in one time step is proved. □

Theorem 3.5. *The solutions of Eqs. (65)–(73) dissipate the time-discretized modified total energy.*

Proof. With the initial condition $R^0 > 0$, we have $R^1 \geq 0$ because the denominator of Eq. (74) is greater than zero. By induction, $R^{n+1} \geq 0$ holds true. From Eq. (72), we derive

$$R^{n+1} - R^n = -\Delta t\left(\frac{R^{n+1}}{E(\mathbf{u}^*, \phi_1^*, \phi_2^*, \phi_3^*) + B_2}\right)\left[\frac{1}{Re}\|\nabla\mathbf{u}^*\|^2 + M\sum_{k=1}^3 \Sigma_k\|\frac{\nabla\mu_k^*}{\Sigma_1}\|^2\right]$$
$$\leq -\Delta t\left(\frac{R^{n+1}}{E(\mathbf{u}^*, \phi_1^*, \phi_2^*, \phi_3^*) + B_2}\right)\left[\frac{1}{Re}\|\nabla\mathbf{u}^*\|^2 + M\overline{\Sigma}\sum_{k=1}^3\|\frac{\nabla\mu_k^*}{\Sigma_k}\|^2\right] \leq 0. \tag{78}$$

Let $\hat{r}^{n+1} = R^{n+1} - B_2$, the above inequality indicates that $\hat{r}^{n+1} \leq \hat{r}^n$ holds. Here, $\hat{r}^{n+1}$ is a modified version of the total energy. The time-discretized modified total energy dissipation law is proved. □

Energy relaxation technique. From Theorem 3.5, we proved the modified energy dissipation law with respect to the modified energy r^{n+1}. To enhance the consistency between the original and modified energies, the following energy relaxation step is adopted:

$$R_o^{n+1} = \xi_0 R^{n+1} + (1 - \xi_0)(E(\mathbf{u}^{n+1}, \phi_1^{n+1}, \phi_2^{n+1}, \phi_2^{n+1}) + B_2),\ \xi_0 \in \chi, \tag{79}$$

where

$$\chi = \left\{\xi_0 \in [0, 1]\ s.t.\ \frac{R_o^{n+1} - R^{n+1}}{\Delta t} \leq -\theta^{n+1}\Psi^{n+1} + \frac{R^{n+1}}{(E(\mathbf{u}^*, \phi_1^*, \phi_2^*, \phi_3^*) + B_2)}\Psi^*\right\}, \tag{80}$$

and $\Psi = \|\nabla\mathbf{u}\|^2/Re + M\sum_{k=1}^3\left(\Sigma_k\|\nabla\frac{\mu_k}{\Sigma_k}\|^2\right)$. We note that χ is not empty because $\xi = 1$ in χ and $\theta^{n+1} \geq 0$. By substituting R_o^{n+1} in Eq. (80) with Eq. (79), we have

$$(R^{n+1} - (E(\mathbf{u}^{n+1}, \phi_1^{n+1}, \phi_2^{n+1}, \phi_3^{n+1}) + B_2))\xi_0 \leq R^{n+1} - (E(\mathbf{u}^{n+1}, \phi_1^{n+1}, \phi_2^{n+1}, \phi_3^{n+1}) + B_2)$$
$$- \Delta t\theta^{n+1}\Psi^{n+1} + \Delta t\frac{R^{n+1}}{(E(\mathbf{u}^*, \phi_1^*, \phi_2^*, \phi_3^*) + B_2)}\Psi^*. \tag{81}$$

The choices of ξ_0 and θ^{n+1} will be described in the following theorem.

Theorem 3.6. *The possible choices of ξ_0 and θ^{n+1} are given as follows:*

Case 1. If $R^{n+1} = (E(\mathbf{u}^{n+1}, \phi_1^{n+1}, \phi_2^{n+1}, \phi_3^{n+1}) + B_2)$, then let $\xi_0 = 0$ and $\theta^{n+1} = \frac{R^{n+1}\Psi^*}{(E(\phi_1^*, \phi_2^*, \phi_3^*) + B_2)\Psi^{n+1}}$;

Case 2. If $R^{n+1} > (E(\mathbf{u}^*, \phi_1^{n+1}, \phi_2^{n+1}, \phi_3^{n+1}) + B_2)$, then let $\xi_0 = 0$ and

$$\theta^{n+1} = \frac{R^{n+1} - (E(\mathbf{u}^{n+1}, \phi_1^{n+1}, \phi_2^{n+1}, \phi_3^{n+1}) + B_2)}{\Delta t \Psi^{n+1}} + \frac{R^{n+1} \Psi^*}{(E(\mathbf{u}^*, \phi_1^*, \phi_2^*, \phi_3^*) + B_2) \Psi^{n+1}};$$

Case 3. If $R^{n+1} < (E(\mathbf{u}^{n+1}, \phi_1^{n+1}, \phi_2^{n+1}, \phi_3^{n+1}) + B_2)$ and

$$R^{n+1} - (E(\mathbf{u}^{n+1}, \phi_1^{n+1}, \phi_2^{n+1}, \phi_3^{n+1}) + B_2) + \Delta t \frac{R^{n+1}}{(E(\mathbf{u}^*, \phi_1^*, \phi_2^*, \phi_3^*) + B_2)} \Psi^* \geq 0,$$

then let $\xi_0 = 0$ and

$$\theta^{n+1} = \frac{R^{n+1} - (E(\mathbf{u}^{n+1}, \phi_1^{n+1}, \phi_2^{n+1}, \phi_3^{n+1}) + B_2)}{\Delta t \Psi^{n+1}} + \frac{R^{n+1} \Psi^*}{(E(\mathbf{u}^*, \phi_1^*, \phi_2^*, \phi_3^*) + B_2) \Psi^{n+1}};$$

Case 4. If $R^{n+1} < (E(\mathbf{u}^{n+1}, \phi_1^{n+1}, \phi_2^{n+1}, \phi_3^{n+1}) + B_2)$ and

$$R^{n+1} - (E(\mathbf{u}^{n+1}, \phi_1^{n+1}, \phi_2^{n+1}, \phi_3^{n+1}) + B_2) + \Delta t \frac{R^{n+1}}{(E(\mathbf{u}^*, \phi_1^*, \phi_2^*, \phi_3^*) + B_2)} \Psi^* < 0,$$

then let $\theta^{n+1} = 0$ and

$$\xi_0 = 1 - \frac{\Delta t R^{n+1} \Psi^*}{(E(\mathbf{u}^*, \phi_1^*, \phi_2^*, \phi_3^*) + B_2)(E(\mathbf{u}^{n+1}, \phi_1^{n+1}, \phi_2^{n+1}, \phi_3^{n+1}) + B_2 - R^{n+1})}.$$

For Cases 1–4, $\xi_0 \in \chi$ and the inequality (81) hold. With $R_o^n \geq 0$ and $R_0^{n+1} \geq 0$, the following inequality is satisfied

$$R_o^{n+1} - R_o^n \leq -\Delta t \theta^{n+1} \Psi^{n+1} \leq 0, \tag{82}$$

which indicates the corrected energy dissipation law. Moreover, $R^{n+1} \leq (E(\mathbf{u}^{n+1}, \phi_1^{n+1}, \phi_2^{n+1}, \phi_3^{n+1}) + B_2)$.

Proof. With ξ_0 and θ^{n+1} defined in all four cases, we have $\xi_0 \in \chi$, i.e., $\xi_0 \in [0, 1]$. As we mentioned in Theorem 3.5, $R^{n+1} \geq 0$ holds true. Moreover, $E(\mathbf{u}^{n+1}, \phi_1^{n+1}, \phi_2^{n+1}, \phi_3^{n+1}) + B_2 \geq 0$ also holds. From Eq. (79), we have $R_o^{n+1} \geq 0$. By combining equalities (72) and (80), we obtain the inequality (82). In Cases 1–3, we have $R_o^{n+1} = (E(\mathbf{u}^{n+1}, \phi_1^{n+1}, \phi_2^{n+1}, \phi_3^{n+1}) + B_2)$ because $\xi_0 = 0$. In Case 4, we know $R^{n+1} \leq (E(\mathbf{u}^{n+1}, \phi_1^{n+1}, \phi_2^{n+1}, \phi_3^{n+1}) + B_2)$ and $\xi_0 \in [0, 1]$, we can derive $R_o^{n+1} \leq (E(\mathbf{u}^{n+1}, \phi_1^{n+1}, \phi_2^{n+1}, \phi_3^{n+1}) + B_2)$ from Eq. (79). The proof is completed. □

In each time iteration, we summarize the numerical implementations as follows

Step 1. Compute R^{n+1} from Eq. (74);
Step 2. Update U^{n+1} and V^{n+1} from Eqs. (71) and (70), respectively;
Step 3. Calculate the intermediate velocity $\tilde{\mathbf{u}}^{n+1}$ from Eq. (65);
Step 4. Calculate p^{n+1} by solving the Poisson equation;
Step 5. Update $\mathbf{u}^{n+1}$ from Eq. (66);
Step 6. Calculate ϕ_k^{n+1} and μ_k^{n+1} ($k = 1, 2$) from Eqs. (68) and (69);
Step 7. Update ϕ_3^{n+1} and μ_3^{n+1} from Eq. (73);
Step 8. Update R_o^{n+1} from Eq. (79);
Step 9. Replace R^{n+1} with R_o^{n+1} and then enter the next time step.

Remark 3.2. By defining the relaxed energy as $r^{n+1} = R_o^{n+1} - B_2$, it is easy to confirm that r^{n+1} is bounded from below because $R_o^{n+1} \geq 0$. In most cases (Cases 1–3), r^{n+1} equals to the time-discretized original energy $E(\mathbf{u}^{n+1}, \phi_1^{n+1}, \phi_2^{n+1}, \phi_3^{n+1})$. Therefore, the energy dissipation law with respect to the relaxed energy r^{n+1} is equivalent to that with respect to the original variable-based energy $E(\mathbf{u}^{n+1}, \phi_1^{n+1}, \phi_2^{n+1}, \phi_3^{n+1})$. For Case 4, the relaxed energy r^{n+1} is an approximation of $E(\mathbf{u}^{n+1}, \phi_1^{n+1}, \phi_2^{n+1}, \phi_3^{n+1})$, and is located in $(\hat{r}^{n+1}, E(\mathbf{u}^{n+1}, \phi_1^{n+1}, \phi_2^{n+1}, \phi_3^{n+1}))$, where $\hat{r}^{n+1}$ is the modified energy defined above. Therefore, the energy relaxation technique leads to the appropriate original variable-based energy dissipation law. Compared with the modified energy dissipation law without relaxation, the consistency is enhanced.

Remark 3.3. The error and convergence analysis of the hydrodynamically coupled phase-field model is an interesting and important problem. Based on the finite difference and finite element methods in space, detailed estimations for the Cahn–Hilliard–Hele–Shaw (CHHS) model were established in [51–53]. An analysis of the second-order accurate finite element scheme on the incompressible Cahn–Hilliard–Navier–Stokes (CHNS) system was developed in [54]. For the ternary CH-type system, Yuan et al. [55] proposed a second-order accurate method and presented a convergence estimation in detail. Recently, error estimations based on SAV-type methods [56,57] were also obtained, especially for the square phase-field crystal model [58] and thin film epitaxial model [59], etc. The present work attempts to design an efficient, linear, and consistently stable time-marching algorithm for the fluid flow-coupled ternary CH system, and validate its capability via extensive simulations. According to a similar idea in [49], the convergence analysis of our proposed scheme will be considered in a separate work.

Table 1
L^2-errors and convergence rates of ϕ_1, ϕ_2, and ϕ_3 with different time steps.

Δt	$32\delta t$		$16\delta t$		$8\delta t$		$4\delta t$		$2\delta t$
ϕ_1:	2.81e-5		7.05e-6		1.73e-6		4.12e-7		8.24e-8
rate		1.99		2.03		2.07		2.32	
ϕ_2:	2.81e-5		7.05e-6		1.73e-6		4.12e-7		8.24e-8
rate		1.99		2.03		2.07		2.32	
ϕ_3:	4.02e-5		1.01e-5		2.47e-6		5.87e-7		1.17e-7
rate		1.99		2.03		2.07		2.32	

Remark 3.4. In [44], Zhang and Yang developed an energy-stable method for the ternary CH model based on the original SAV scheme. Although the original SAV technique leads to a linear time-marching scheme, the phase-field and time-dependent auxiliary variables are coupled in time. In each time step, a splitting technique is required to achieve a totally decoupled computation. Please refer to [44] for a detailed description of the implementation. However, the original SAV method generally has higher computational costs because it splits one original equation into two subproblems. By applying the original SAV method to the hydrodynamically coupled ternary CH system [60], the computational costs further increase because additional splitting is required for the velocities. By introducing a time-dependent auxiliary variable related to the free and kinetic energies, we recast the original system into a novel equivalent form. Based on the equivalent equations, the resulting scheme is more efficient because all the variables (phase-field function, velocity, and auxiliary variable) are completely decoupled. Therefore, there is no need to apply the splitting technique, and the computational cost is similar to that of the classical linear semi-implicit scheme. In terms of robustness, the original SAV method [44] and the proposed method multiply the nonlinear terms with the appropriate variable. With the refinement of the time step, this variable converges to 1. Thus, the behaviors of the original and proposed SAV methods are similar to that of the classical linear semi-implicit scheme. The computational stability is mainly affected by the intensity of the stabilization term. Therefore, the robustness of the proposed scheme is analogous to that of the original SAV method.

4. Numerical experiments

Extensive numerical simulations are conducted to verify the accuracy, stability, and performance of the proposed scheme. Spatial discretization is conducted using the finite difference method (FDM). The resulting elliptic equations are solved by a fast multigrid algorithm [61]. In 2D space, the zero Neumann boundary condition is used for ϕ_k, μ_k ($k = 1, 2, 3$), and p along the y-direction. The no-slip boundary condition is considered for $\mathbf{u}$ at the upper and bottom boundaries. Along the x-direction, the periodic boundary condition is used for all variables. In 3D space, a periodic boundary condition is used for all variables along the x- and y-directions. At the upper and bottom boundaries, the zero Neumann boundary condition is applied for ϕ_k, μ_k ($k = 1, 2, 3$), and p; and the no-slip boundary condition is applied for $\mathbf{u}$.

4.1. Temporal accuracy in the absence of fluid

First, we study the temporal accuracy of our proposed scheme for the three-component CH in the absence of fluid flows. The computational domain is set as $\Omega = (0, 2) \times (0, 2)$. The mesh size of 256×256 is fixed. We consider the following initial conditions:

$$\phi_1(x, y, 0) = \frac{1}{2} + \frac{1}{2}\tanh\left(\frac{0.23 - \sqrt{(x - 1.25)^2 + (y - 1)^2}}{\epsilon}\right), \tag{83}$$

$$\phi_2(x, y, 0) = \frac{1}{2} + \frac{1}{2}\tanh\left(\frac{0.23 - \sqrt{(x - 0.75)^2 + (y - 1)^2}}{\epsilon}\right), \tag{84}$$

$$\phi_3(x, y, 0) = 1 - \phi_1(x, y, 0) - \phi_2(x, y, 0). \tag{85}$$

The parameters are set as $\epsilon = 0.018$, $\sigma_{12} = \sigma_{13} = \sigma_{23} = 1$, $\Lambda = 1.5$, and $M = 0.01$. The stabilization parameter $S = 30$ is adopted. In the next subsection, we will investigate the selection of the appropriate S through comparison studies. A sufficient time step $\delta t = 0.01h^2$ is considered to calculate the numerical reference solutions. Here, $h = 1/128$ is the space step. The convergent numerical solutions of ϕ_k ($k = 1, 2, 3$) are computed using different time steps: $\Delta t = 32\delta t$, $16\delta t$, $8\delta t$, $4\delta t$, and $2\delta t$. By comparison with the reference solutions, Table 1 lists the L^2-errors and corresponding convergence rates with respect to ϕ_1, ϕ_2, and ϕ_3. The results confirm that the proposed method achieves temporally second-order accuracy.

4.2. Effect of stabilization parameter

To suppress the effect of explicit nonlinear terms and enhance the numerical stability, the stabilization term, i.e., $S\Sigma_k(\phi_k^{n+1} - \phi_k^*)$ is added. Here, S is an empirical positive constant that should be properly chosen. In this subsection, we investigate an appropriate value of S by considering the evolution of the energy curves at different time steps because the energy dissipation is a basic property. We set the domain and mesh size as $\Omega = (0, 2) \times (0, 2)$ and 256×256, respectively. The initial conditions are set as

$$\phi_1(x, y, 0) = \frac{1}{3} + 0.01\text{rand}(x, y), \tag{86}$$
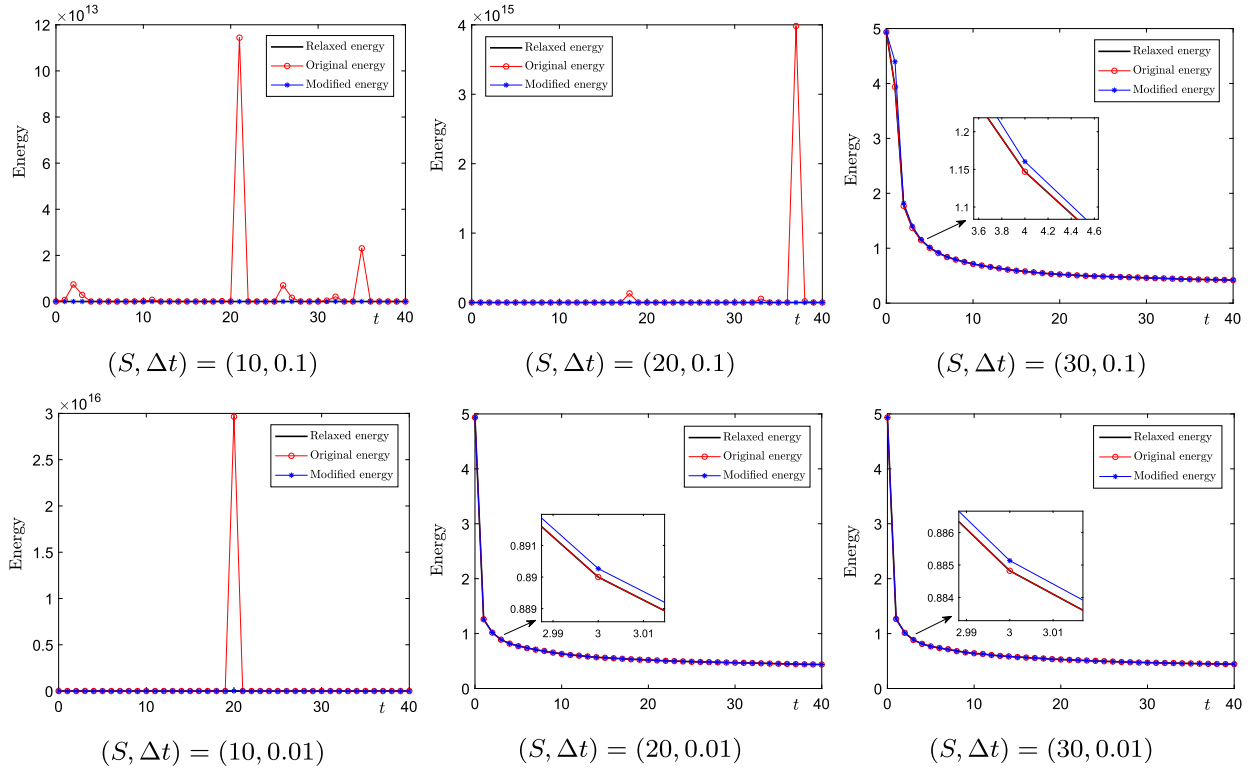
Fig. 1. Relaxed, original, and modified energy curves with respect to $S = 10$ (left), $S = 20$ (middle), and $S = 30$ (right). The top and bottom rows correspond to $\Delta t = 0.1$ and $\Delta t = 0.01$, respectively.
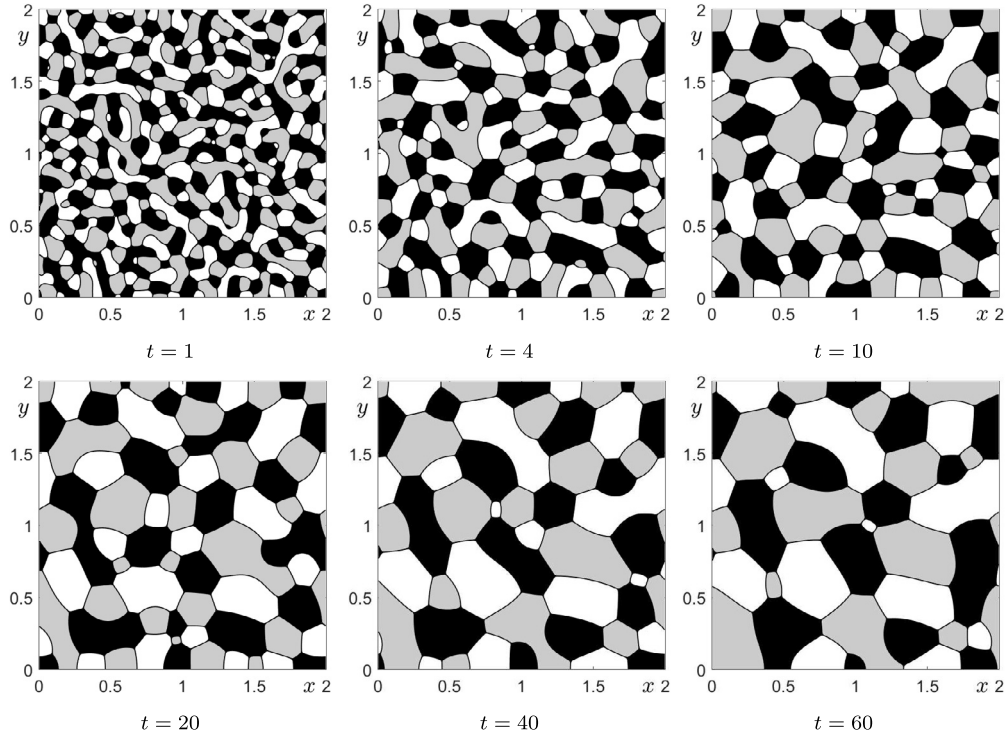
Fig. 2. Snapshots of ternary phase separation with $\Delta t = 0.01$. The black, gray, and white regions are occupied by ϕ_1, ϕ_2, and ϕ_3, respectively.

$$\phi_2(x, y, 0) = \frac{1}{3} + 0.01\text{rand}(x, y), \tag{87}$$

$$\phi_3(x, y, 0) = 1 - \phi_1(x, y, 0) - \phi_2(x, y, 0), \tag{88}$$

where rand(x, y) is a random number between -1 and 1. The parameters $\epsilon = 0.018$, $\sigma_{12} = \sigma_{13} = \sigma_{23} = 1$, $\Lambda = 1.5$, and $M = 0.01$ are used. The top and bottom rows in Fig. 1 correspond to the results with respect to $\Delta t = 0.1$ and 0.01. From left to right in each row, the
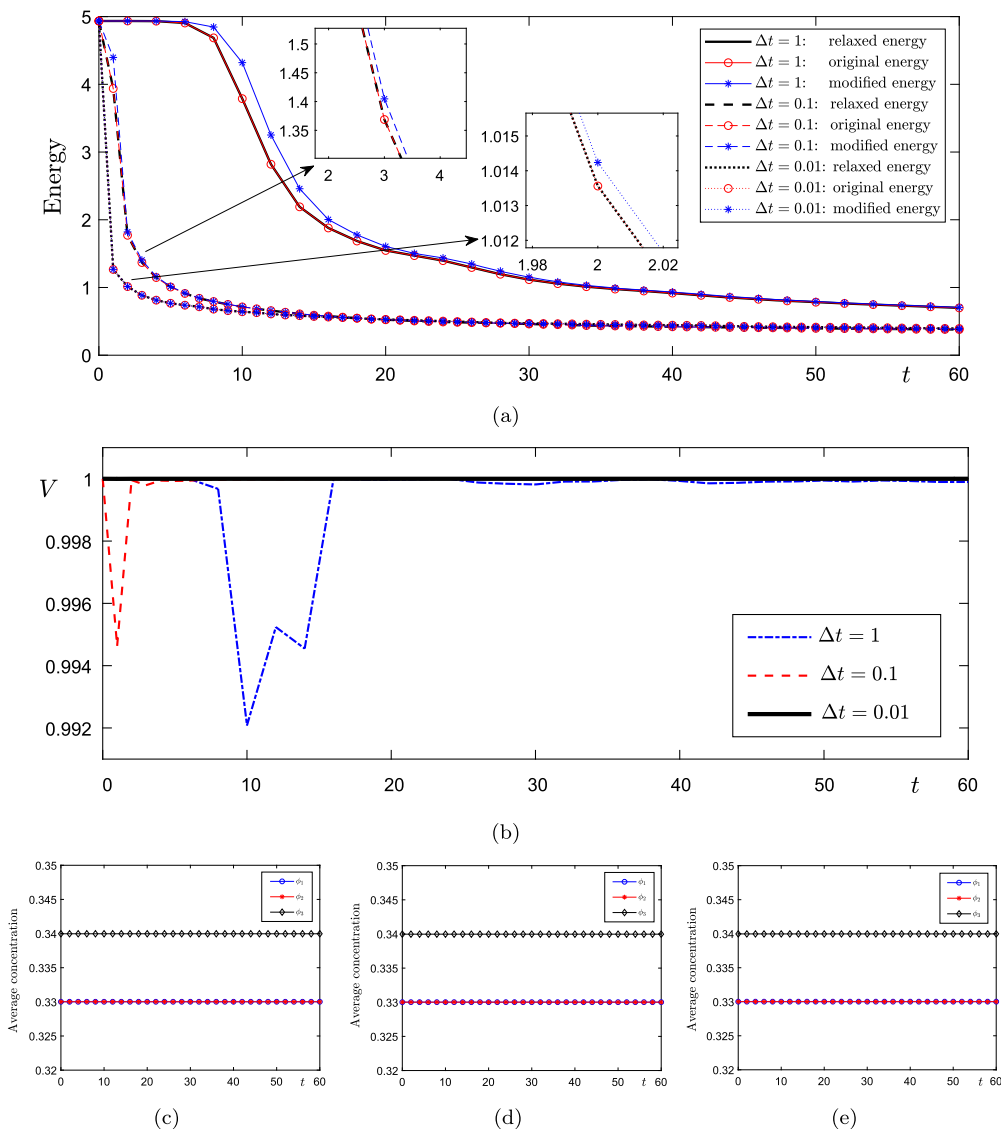
Fig. 3. Energy curves with respect to different time steps. (a) Evolution of V for different time steps. (b) Evolutions of average concentrations with respect to (c) $\Delta t = 1$, (d) $\Delta t = 0.1$, and (e) $\Delta t = 0.01$.

evolution of the relaxed energy r^n, original energy $E(\phi_1^n, \phi_2^n, \phi_3^n)$, and modified energy $\hat{r}^n$ are plotted. When $S = 10$, the original energy does not dissipate monotonically despite the use of the small time step $\Delta t = 0.01$. When $S = 20$ and $\Delta t = 0.1$, the energy dissipation property of the original energy is not satisfied. When a smaller time step $\Delta t = 0.01$ is used, the relaxed, original, and modified energies decrease over time. When $S = 30$, the relaxed, original, and modified energies dissipate monotonically despite the use of a larger time step. The numerical results indicate that small stabilization parameters could not suppress the stiffness caused by the explicit nonlinear terms. In the following simulations, we will adopt $S = 30$ without any specific needs. The monotonically dissipative energy curves also indicate that the original and relaxed energies are in good agreement. The relaxation technique enhances the consistency.

4.3. Energy dissipation property

In the previous section, we proved that the proposed scheme, equipped with the appropriate stabilization term, satisfies the unconditional energy dissipation laws with respect to the modified and relaxed energies. To confirm this result via numerical simulations, we consider three different time steps: $\Delta t = 1$, 0.1, and 0.01. The computational domain, mesh size, initial conditions, and other parameters remain unchanged. Fig. 2 displays snapshots of the ternary phase separation obtained using $\Delta t = 0.01$. Here, the same surface tension coefficients, i.e., $\sigma_{12} = \sigma_{13} = \sigma_{23} = 1$ are considered. The black, gray, and white regions are occupied by ϕ_1, ϕ_2, and ϕ_3, respectively. With time evolution, we find that the same materials merge with each other. These three components occupy approximately the same proportion of the domain. Fig. 3(a) plots the evolution of the relaxed, original, and modified energies with respect to different time steps. It can be observed that the energy curves do not increase with time. With the refinement of the time step, the energy evolutions converge. This indicates that a fine time step is necessary to obtain accurate numerical results. Moreover, the results also indicate that the energy relaxation technique increases the consistency between the original and relaxed energies. In Fig. 3(b), the evolutions of V at different time steps are plotted. We find that V is close to the exact value 1. In particular, the values of V and 1 are consistent when a fine time step is
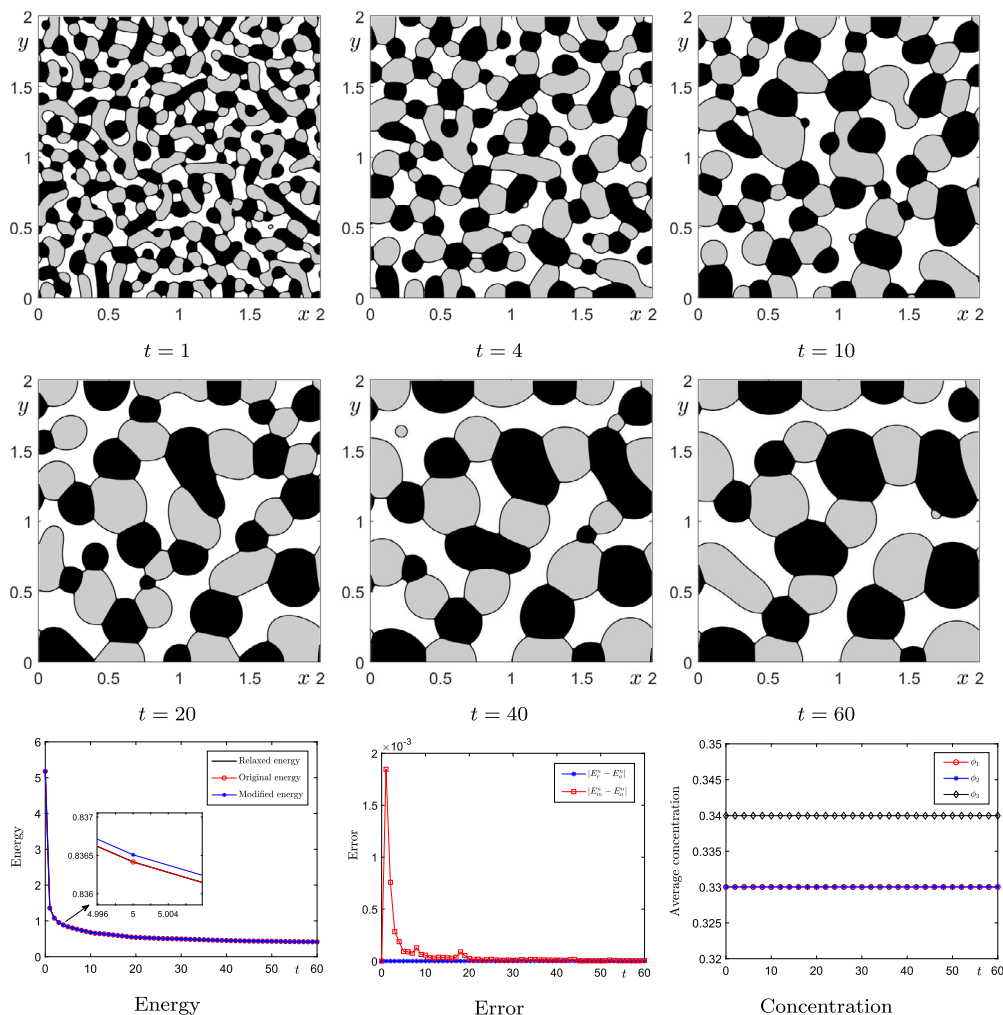
Fig. 4. The top and bottom rows show the snapshots of ternary phase separation with $(\sigma_{12}, \sigma_{13}, \sigma_{23}) = (1, 0.8, 1.4)$. The bottom row plots the evolutions of the energy curves, relative errors, and average concentrations.

used. In Figs. 3(c)–(e), the evolutions of the average concentrations with respect to $\Delta t = 1, 0.1$, and 0.01 are plotted. It can be seen that the mass conservation is satisfied at each time step.

4.4. Ternary phase separation without fluid

For a homogeneously distributed three-component system, the initial perturbations lead to the spontaneous growth of the concentrations. With time evolution, three-component states are formed. This process is called the ternary phase separation. It should be noted that this process generally dissipates the free energy owing to the decrease in the total interfacial length. Furthermore, the surface tension also affects the evolution dynamics. In this subsection, we study the effects of surface tension on the evolution of ternary patterns and the corresponding energy dissipation properties. The domain and mesh size are set as $\Omega = (0, 2) \times (0, 2)$ and 256×256, respectively. The random initial conditions in subsection 4.2 are used. We consider $\Delta t = 0.01$, $\epsilon = 0.018$, $M = 0.01$, $\Lambda = 1.5$, and $S = 30$. The top and middle rows in Fig. 4 show snapshots of the ternary phase separation with $(\sigma_{12}, \sigma_{13}, \sigma_{23}) = (1, 0.8, 1.4)$, where the black, gray, and white regions are occupied by ϕ_1, ϕ_2, and ϕ_3, respectively. It can be seen that ϕ_1 and ϕ_2 are linked to each other to form the chain pattern; the remaining regions are occupied by ϕ_3. The bottom row in Fig. 4 displays the evolutions of the energy curves, relative errors between the original energy and relaxed/modified energy, and average concentrations. It should be noted that $E_o^n = E(\phi_1^n, \phi_2^n, \phi_3^n)$ is the time-discretized original energy; we use E_o^n to simplify the notation. The time-discretized modified and relaxed energies are $E_m^n = \hat{r}^n$ and $E_r^n = r^n$, respectively. The results indicate that the energy curves do not increase with time. The relaxed and original energies are in good agreement. The average concentrations are conserved. The top and middle rows in Fig. 5 show snapshots of the ternary phase separation with $(\sigma_{12}, \sigma_{13}, \sigma_{23}) = (1, 1, 3)$. The top and middle rows in Fig. 6 show snapshots of the ternary phase separation with $(\sigma_{12}, \sigma_{13}, \sigma_{23}) = (3, 1, 1)$. In these two cases, the three components evolve over time to form separate droplet patterns. From the results plotted in the bottom rows in Figs. 5 and 6, it can be seen that the energy curves decrease with time, the original and relaxed energies are in good agreement, and the average concentrations are conserved. These simulations not only show that the surface tension coefficients have significant effect on the evolutionary dynamics of ternary phase separation, but also indicate that the proposed method can preserve the energy dissipation law and mass of each component. In Figs. 4–6, the phase separations are simulated until a steady state is achieved. In early stage, phase transition rapidly occurs, leading to an obvious change in the energy functional. Bulk phases appear when the ternary materials evolve past the transition state. Afterwards, the coarsening dynamics becomes dominant, and the same fluids merge with each
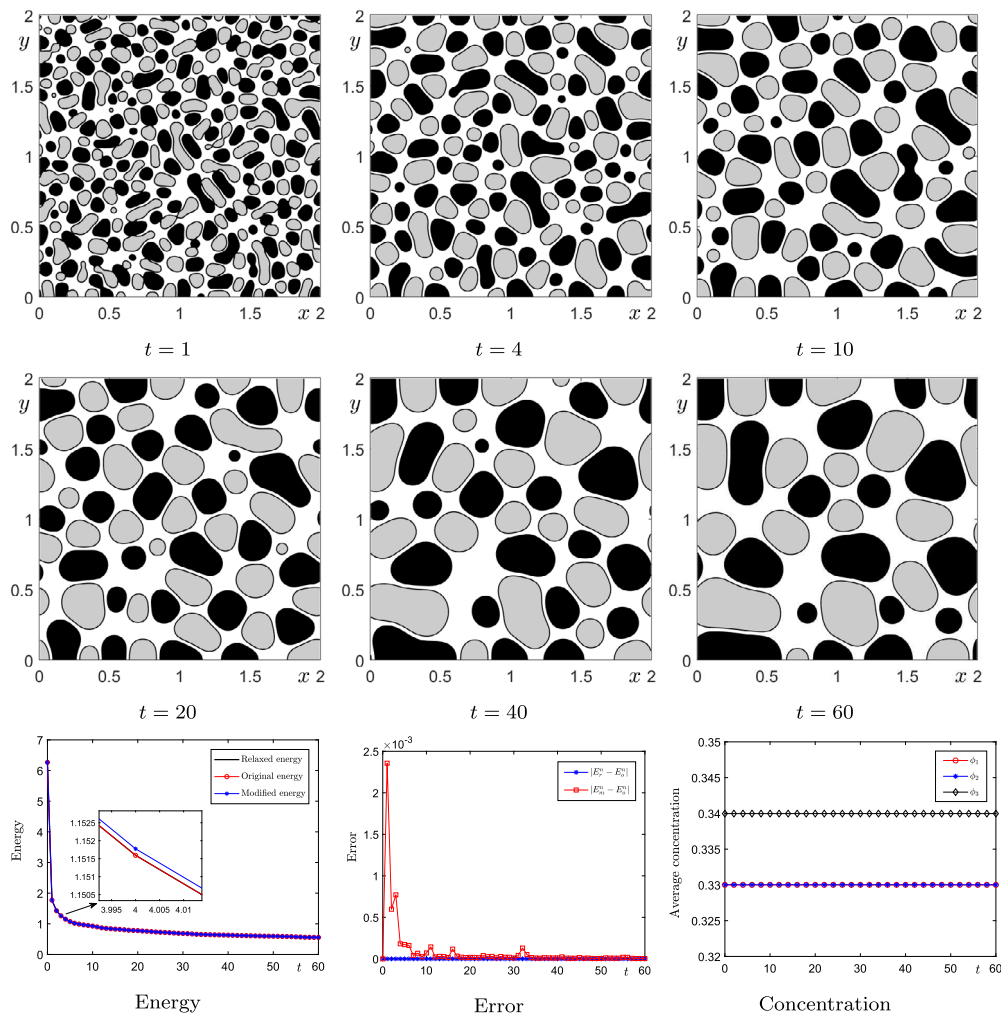
Fig. 5. The top and middle rows show the snapshots of ternary phase separation with $(\sigma_{12}, \sigma_{13}, \sigma_{23}) = (1, 1, 3)$. The bottom row plots the evolutions of the energy curves, relative errors, and average concentrations.

other to occupy most of the regions. Although this process generally takes a long time to achieve the steady state, the energy tends to be flat. This explains why the energy curves approximately converge over time. The same phenomena have been widely reported in previous studies [18–21,44].

4.5. Two adjacent droplets with different sizes

Previous studies tested the effects of surface tension on the dynamics of two droplets with the same size. The total and partial spreading phenomena were observed by adjusting the surface tension coefficients. In this subsection, we conduct similar simulations of two adjacent droplets with different sizes. We consider the computational domain $\Omega = (0, 2) \times (0, 2)$ with the mesh size 256×256. The initial states are defined as follows:

$$\phi_1(x, y, 0) = \frac{1}{2} + \frac{1}{2} \tanh\left(\frac{0.34 - \sqrt{(x - 0.85)^2 + (y - 0.85)^2}}{\epsilon}\right), \tag{89}$$

$$\phi_2(x, y, 0) = \frac{1}{2} + \frac{1}{2} \tanh\left(\frac{0.2 - \sqrt{(x - 1.25)^2 + (y - 1.25)^2}}{\epsilon}\right), \tag{90}$$

$$\phi_3(x, y, 0) = 1 - \phi_1(x, y, 0) - \phi_2(x, y, 0). \tag{91}$$

The parameters used in the previous subsection are adopted. The top and middle rows in Fig. 7 show the snapshots with respect to $(\sigma_{12}, \sigma_{13}, \sigma_{23}) = (1, 1, 1)$. The top and middle rows in Fig. 8 show the snapshots with respect to $(\sigma_{12}, \sigma_{13}, \sigma_{23}) = (1, 0.8, 1.4)$. The top and middle rows in Fig. 9 show the snapshots with respect to $(\sigma_{12}, \sigma_{13}, \sigma_{23}) = (1, 1, 3)$. In all the figures, the white, black, and gray regions are occupied by ϕ_1, ϕ_2, and ϕ_3, respectively. For $(\sigma_{12}, \sigma_{13}, \sigma_{23}) = (1, 1, 1)$ and $(1, 0.8, 1.4)$, the spreading is partial. Their evolutionary shapes are slightly different owing to the equal and unequal distributions of the surface tension. For $(\sigma_{12}, \sigma_{13}, \sigma_{23}) = (1, 1, 3)$, the spreading is total. With the time evolution, we observe that ϕ_2 moves into ϕ_1 because ϕ_1 totally spreads out. At the bottom rows in Figs. 7, 8, and 9, the evolutions of the energy curves, relative errors, and average concentrations are plotted. For each case, we can observe that the
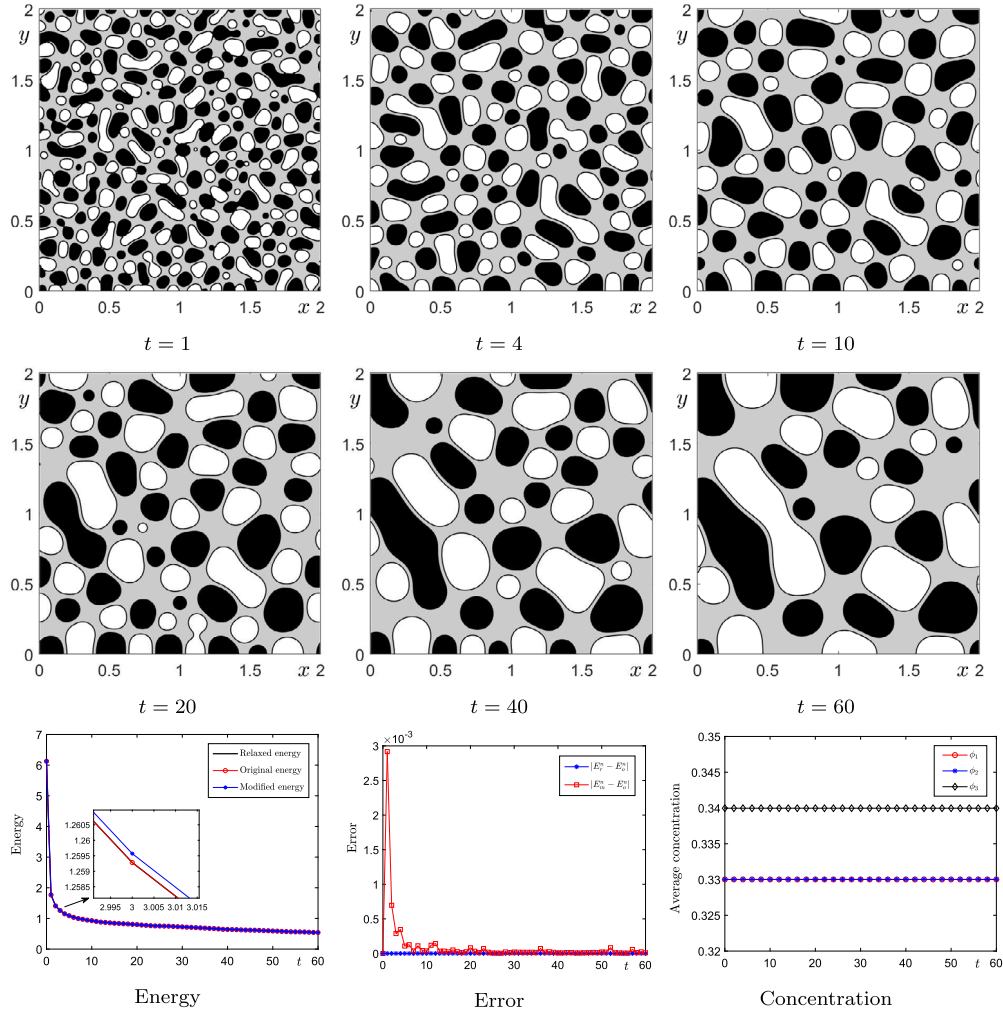
Fig. 6. The top and middle rows show the snapshots of ternary phase separation with $(\sigma_{12}, \sigma_{13}, \sigma_{23}) = (3, 1, 1)$. The bottom row plots the evolutions of the energy curves, relative errors, and average concentrations.

energy curves are decreasing with time, the relaxed energy and original energy are in better agreement, and the average concentrations are conserved.

4.6. Temporal accuracy with fluid

In this subsection, we investigate the temporal accuracy of the numerical method for the flow-coupled ternary CH system. The initial conditions [45] are as follows:

$$\phi_1(x, y, 0) = 0.5 + 0.5 \tanh \left(\frac{0.3 - \sqrt{(x-1)^2 + (y-0.5)^2}}{\epsilon} \right),$$

$$\phi_2(x, y, 0) = (1 - \phi_1(x, y, 0)) \left(0.5 + 0.5 \tanh \left(\frac{y - 0.5}{\epsilon} \right) \right),$$

$$\phi_3(x, y, 0) = 1 - \phi_1(x, y, 0) - \phi_2(x, y, 0),$$

$$u(x, y, 0) = v(x, y, 0) = 0, \quad p(x, y, 0) = 0.$$

The domain is set as $\Omega = (0, 2) \times (0, 1)$. The parameters $M = 0.001$, $\sigma_{12} = \sigma_{13} = \sigma_{23} = 1$, $\epsilon = 0.018$, $\Lambda = 1.5$, $S = 30$, and $Re = 1$ are used. The numerical reference solutions are obtained using the fine time step $\delta t = 0.01h^2$, where $h = 1/128$ is the space step. The comparisons are computed by increasing the reference time step by a factor of two until $\Delta t = 32\delta t$. The L^2-errors and convergence rates for all variables are listed in Table 2. The computational results show that our proposed time-marching method achieves temporally second-order accuracy.

4.7. Hydrodynamically coupled phase separation

The simulations in subsection 4.4 show that the surface tension significantly affects the phase separation dynamics. The existence of fluid flows also leads to different evolutionary processes. In this subsection, we study the effects of surface tension by considering the ternary phase separation with $(\sigma_{12}, \sigma_{13}, \sigma_{23}) = (1, 1, 1)$, $(1, 0.8, 1.4)$, and $(3, 1, 1)$. The computational domain, mesh size, and random
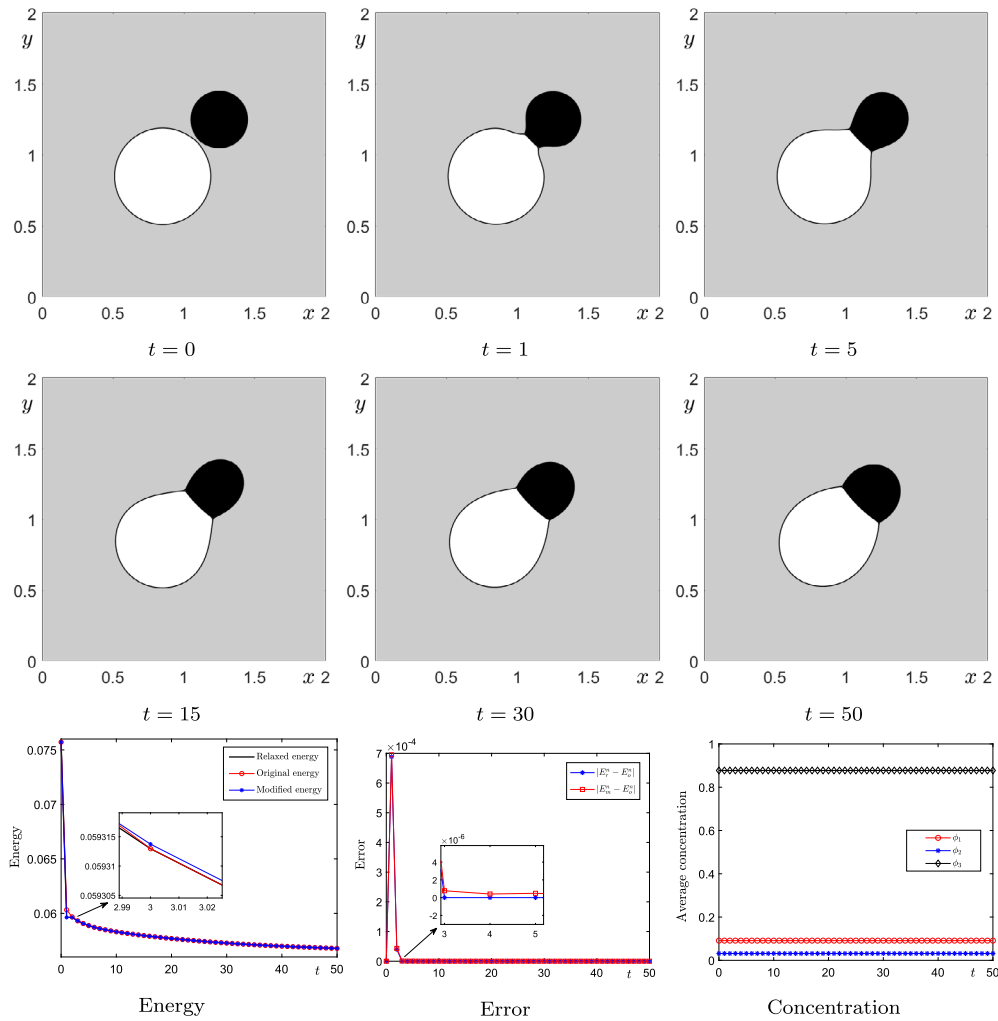
Fig. 7. The top and middle rows show the snapshots of two adjacent droplets with $(\sigma_{12}, \sigma_{13}, \sigma_{23}) = (1, 1, 1)$. The bottom row plots the evolutions of the energy curves, relative errors, and average concentrations.

Table 2
L^2-errors and convergence rates for ϕ_k, $(k = 1, 2, 3)$, u, and v with different time steps.

Δt	$32\delta t$		$16\delta t$		$8\delta t$		$4\delta t$		$2\delta t$
ϕ_1:	6.11e-7		1.54e-7		3.82e-8		9.09e-9		1.82e-9
rate		1.98		2.02		2.07		2.32	
ϕ_2:	6.02e-7		1.52e-7		3.77e-8		8.97e-9		1.79e-9
rate		1.98		2.02		2.07		2.32	
ϕ_3:	6.02e-7		1.52e-7		3.77e-8		8.97e-9		1.79e-9
rate		1.98		2.02		2.07		2.32	
u:	8.55e-8		1.91e-8		4.64e-9		1.08e-9		2.15e-10
rate		2.17		2.04		2.10		2.34	
v:	6.63e-8		1.47e-8		3.55e-9		8.28e-10		1.64e-10
rate		2.17		2.05		2.10		2.34	

initial conditions of ϕ_k $(k = 1, 2, 3)$ in subsection 4.2 are used. The initial velocity field and pressure are set to zero. The parameters are set as $\Delta t = 0.01$, $\epsilon = 0.018$, $M = 0.01$, $Re = 1$, $\Lambda = 1.5$, and $S = 30$. Figs. 10, 11, and 12 show snapshots of hydrodynamically coupled three-component phase separation with respect to $(\sigma_{12}, \sigma_{13}, \sigma_{23}) = (1, 1, 1)$, $(1, 0.8, 1.4)$, and $(3, 1, 1)$, respectively. The black, gray, and white regions are occupied by ϕ_1, ϕ_2, and ϕ_3. The velocity field is represented by the blue arrows. The results in Figs. 10 and 11 correspond to the partially spreading phenomena. Owing to the equal and unequal distributions of the surface tension, the contact angles in the triple junctions are different. At the initial stage, the velocities are zero and these evolve over time owing to the driving effect of the surface tension. As the coarsening process reaches an equilibrium state, the velocity field dissipates its energy. This is reflected in the figures showing the decreasing size of the velocity arrows. In the totally spreading case, i.e., $(\sigma_{12}, \sigma_{13}, \sigma_{23}) = (3, 1, 1)$, the three components evolve to form some separately distributed droplets. The triple junctions do not appear because the phase is totally spread out. Similarly, the velocities evolve over time and gradually dissipate as the system reaches the equilibrium state. The top and bottom rows in Fig. 13
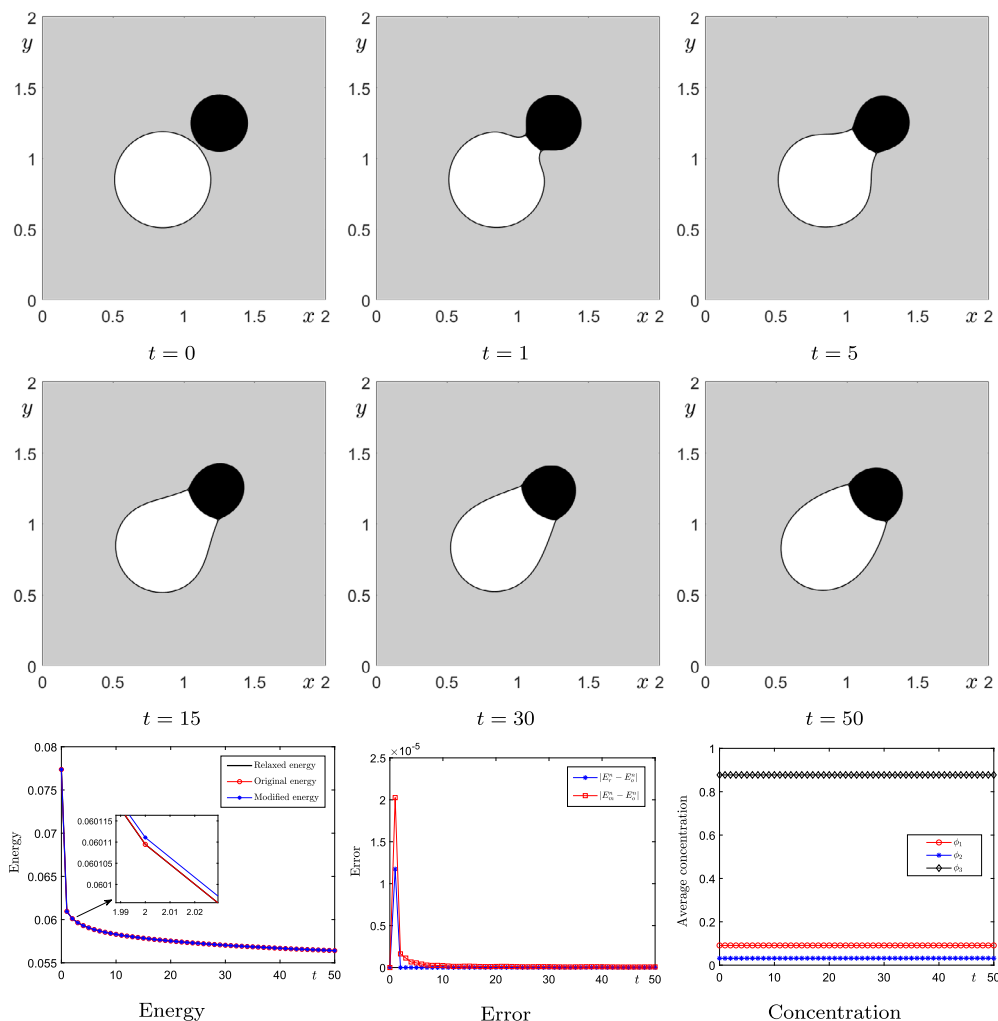
Fig. 8. The top and middle rows show the snapshots of two adjacent droplets with $(\sigma_{12}, \sigma_{13}, \sigma_{23}) = (1, 0.8, 1.4)$. The bottom row plots the evolutions of the energy curves, relative errors, and average concentrations.

show the evolutions of the energy curves and average concentrations. The figures from left to right correspond to $(\sigma_{12}, \sigma_{13}, \sigma_{23}) = (1, 1, 1)$, $(1, 0.8, 1.4)$, and $(3, 1, 1)$, respectively. It can be observed that the energy curves decrease with time, and the average concentrations are conserved.

4.8. Two droplets in shear flow

In simple shear flow, the droplets deform under the combined effects of the velocity field and surface tension. Many researchers have used the droplet deformation in simple shear flow as a benchmark; please refer to [45,62,63] for simulations using the phase-field method. To simulate the droplet dynamics in a simple shear flow under different surface tension coefficients, we set the domain as $\Omega = (0, 2) \times (0, 1)$. The mesh size of 256×128 is considered. The initial states are defined as follows:

$$\phi_1(x, y, 0) = \frac{1}{2} + \frac{1}{2} \tanh\left(\frac{0.25 - \sqrt{(x - 1.26)^2 + (y - 0.4)^2}}{\epsilon} \right), \tag{92}$$

$$\phi_2(x, y, 0) = \frac{1}{2} + \frac{1}{2} \tanh\left(\frac{0.25 - \sqrt{(x - 0.74)^2 + (y - 0.6)^2}}{\epsilon} \right), \tag{93}$$

$$\phi_3(x, y, 0) = 1 - \phi_1(x, y, 0) - \phi_2(x, y, 0), \tag{94}$$

$$u(x, y, 0) = (y - 0.5)/2, \ v(x, y, 0) = 0, \ p(x, y, 0) = 0. \tag{95}$$

The initial profiles are shown in Fig. 14(a). The gray, black, and white regions are occupied by ϕ_1, ϕ_2, and ϕ_3, respectively. We set $\Delta t = 0.001$, $\epsilon = 0.018$, $\Lambda = 1.5$, $M = 0.01$, $Re = 1$, and $S = 30$. The velocities are represented by the blue arrows. Under the driving effect of the initial velocity field, the initially separated droplets deform over time. The deformation is affected by different surface tensions. Fig. 15 shows the snapshots with respect to $(\sigma_{12}, \sigma_{13}, \sigma_{23}) = (4, 4, 4)$. We find that the two droplets are bound together with identical shapes owing to the equal surface tension effect. Fig. 16 shows the snapshots with respect to $(\sigma_{12}, \sigma_{13}, \sigma_{23}) = (4, 3.2, 5.6)$. Because of the unequal surface tension effect, we observe that the droplet occupied by ϕ_1 is stretched. The evolutions with respect to
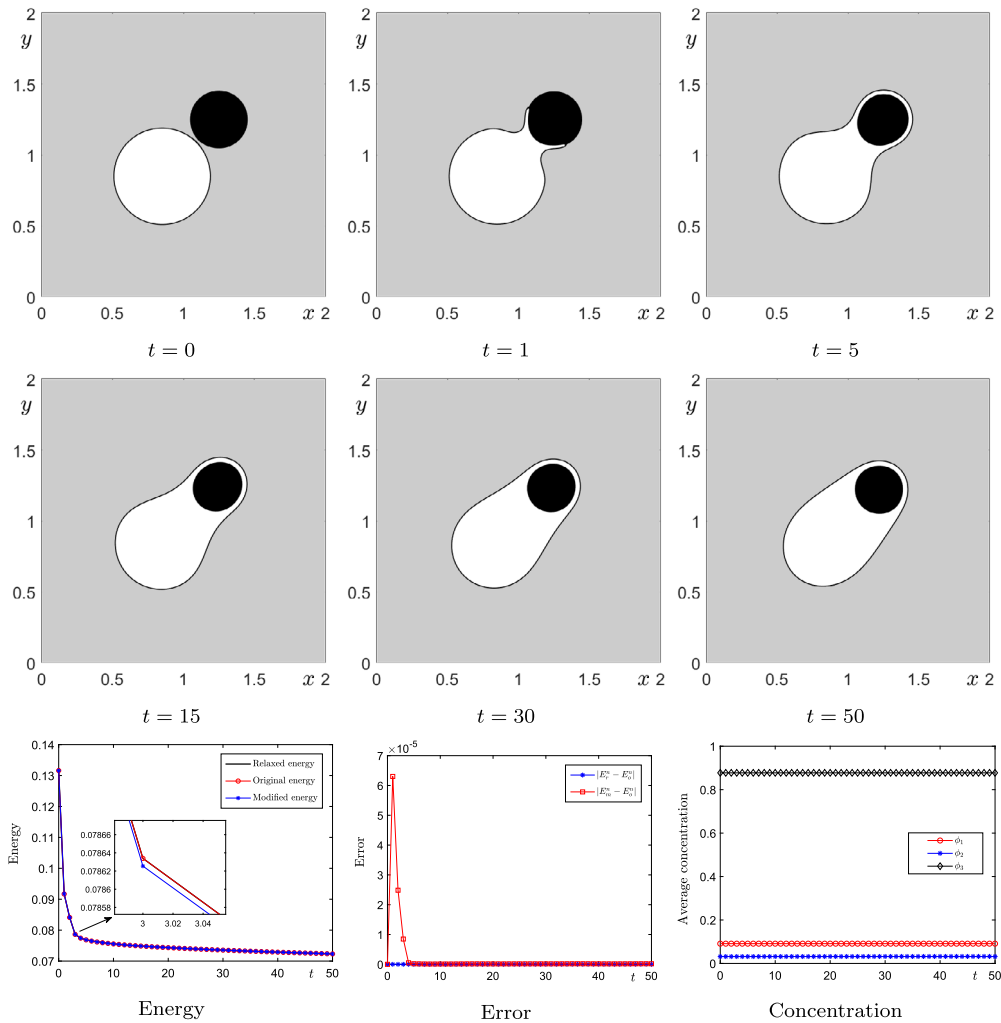
Fig. 9. The top and middle rows show the snapshots of two adjacent droplets with $(\sigma_{12}, \sigma_{13}, \sigma_{23}) = (1, 1, 3)$. The bottom row plots the evolutions of the energy curves, relative errors, and average concentrations.

$(\sigma_{12}, \sigma_{13}, \sigma_{23}) = (12, 4, 4)$ are shown in Fig. 17. In the totally spreading case, the two droplets remain separated. The numerical results indicate that the surface tension generally has an obvious effect on the droplet dynamics in shear flow.

4.9. Ternary liquid lens in simple shear flow

When an initially circular droplet is located at the interface between two immiscible fluids, the surface tension causes the droplet to deform. This process is affected by different surface tension coefficients and the velocity field. In this subsection, we study the evolutionary dynamics of liquid lenses with different surface tension coefficients in simple shear flow. The initial states are shown in Fig. 14(b). The white, gray, and black regions are occupied by ϕ_1, ϕ_2, and ϕ_3, respectively. The other parameters remain unchanged. The left and right columns in Fig. 18 display the snapshots of the liquid lens with respect to $(\sigma_{12}, \sigma_{13}, \sigma_{23}) = (4, 4, 4)$ and $(4, 3.2, 5.6)$, respectively. With the equal surface tension effect (i.e., $(\sigma_{12}, \sigma_{13}, \sigma_{23}) = (4, 4, 4)$), it can be observed that the liquids occupied by ϕ_2 and ϕ_3 share the identical interfacial shapes. With the equal surface tension effect (i.e., $(\sigma_{12}, \sigma_{13}, \sigma_{23}) = (4, 3.2, 5.6)$), most parts of the droplet are covered by the liquid occupied by ϕ_2. This phenomenon is attributed to the unequal surface tension effect. The left column in Fig. 19 shows the snapshots of the liquid lens with respect to $(\sigma_{12}, \sigma_{13}, \sigma_{23}) = (4, 4, 12)$. We find that the droplet completely moves into the liquid phase occupied by ϕ_2 and then deforms owing to the shear flow. The right column in Fig. 19 shows the snapshots of the liquid lens with respect to $(\sigma_{12}, \sigma_{13}, \sigma_{23}) = (12, 4, 4)$. It can be observed that the initial droplet is totally stretched. The different surface tension coefficients also have a significant effect on the velocity evolutions.

4.10. Falling droplet in a ternary fluid system

Finally, we consider the ternary fluid system under the combined effects of gravity and surface tension. A heavy droplet (ϕ_1) is initially located at the upper position of the interface between lighter liquids ϕ_2 and ϕ_3. Under the driving effect of gravity, the droplet falls and penetrates the interface. By considering the Boussinesq approximation [64], the momentum equation is expressed as

$$\tilde{\rho}\left(\frac{\partial \mathbf{u}}{\partial t} + \mathbf{u} \cdot \nabla \mathbf{u}\right) = -\nabla p + \frac{1}{Re}\Delta \mathbf{u} - \sum_{k=1}^{3}\phi_k \nabla \mu_k + (\rho(\phi_1, \phi_2, \phi_3) - \tilde{\rho})\mathbf{g}, \tag{96}$$
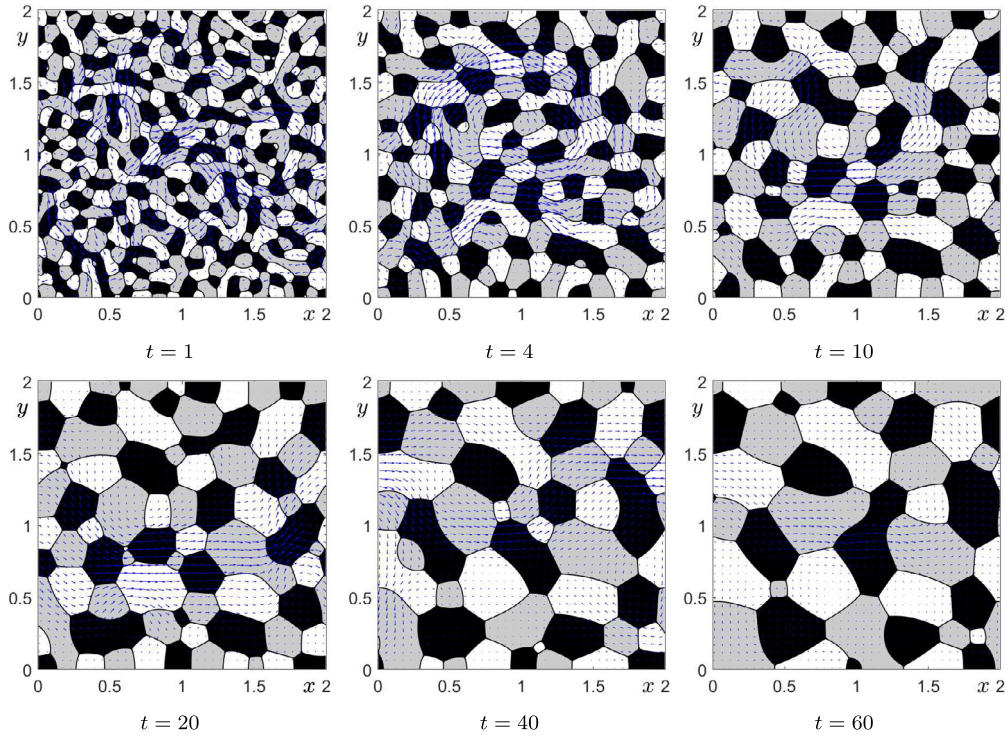
Fig. 10. Snapshots of flow-coupled ternary phase separation with respect to $(\sigma_{12}, \sigma_{13}, \sigma_{23}) = (1, 1, 1)$. (For interpretation of the colors in the figure(s), the reader is referred to the web version of this article.)
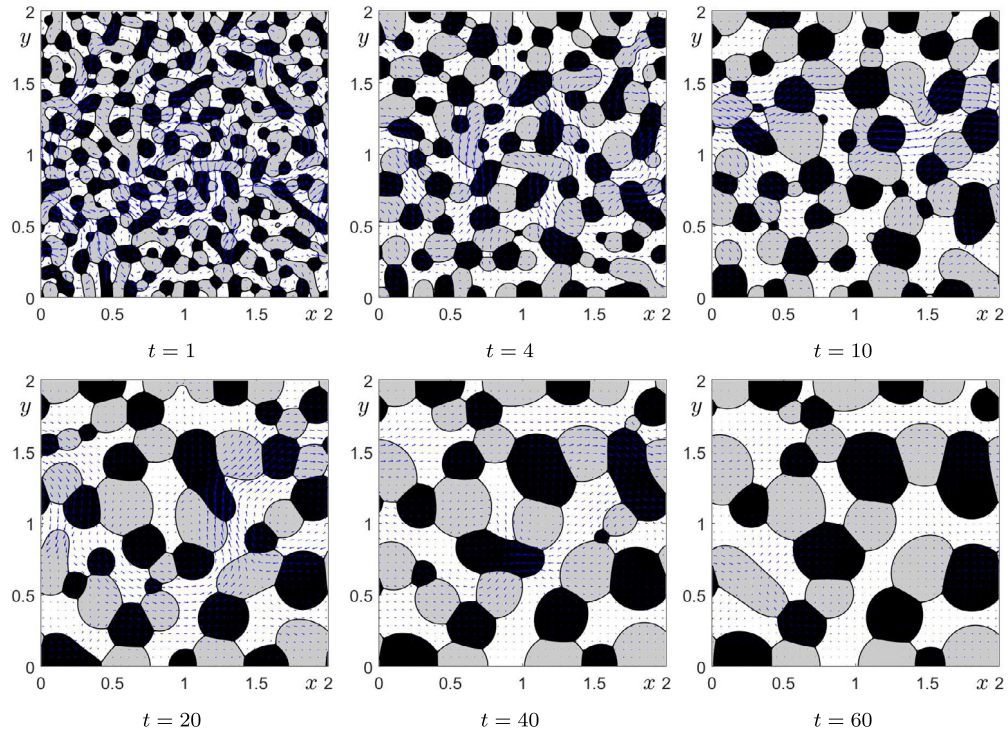
Fig. 11. Snapshots of flow-coupled ternary phase separation with respect to $(\sigma_{12}, \sigma_{13}, \sigma_{23}) = (1, 0.8, 1.4)$.

where $\rho(\phi_1, \phi_2, \phi_3) = \sum_{k=1}^{3} \rho_k \phi_k$ and ρ_k are the densities of k-th component. Here, $\tilde{\rho}$ is the reference value and $\tilde{\rho} = \rho_1$. The gravity is $\mathbf{g} = (0, -g)$ and $\mathbf{g} = (0, 0, -g)$ in 2D and 3D spaces, respectively. For the 2D simulation, we consider the domain $\Omega = (0, 2) \times (0, 4)$, mesh size 128×256, and the following initial conditions:

$$\phi_1(x, y, 0) = \frac{1}{2} + \frac{1}{2} \tanh \left(\frac{0.25 - \sqrt{(x-1)^2 + (y-3.4)^2}}{\epsilon} \right), \tag{97}$$
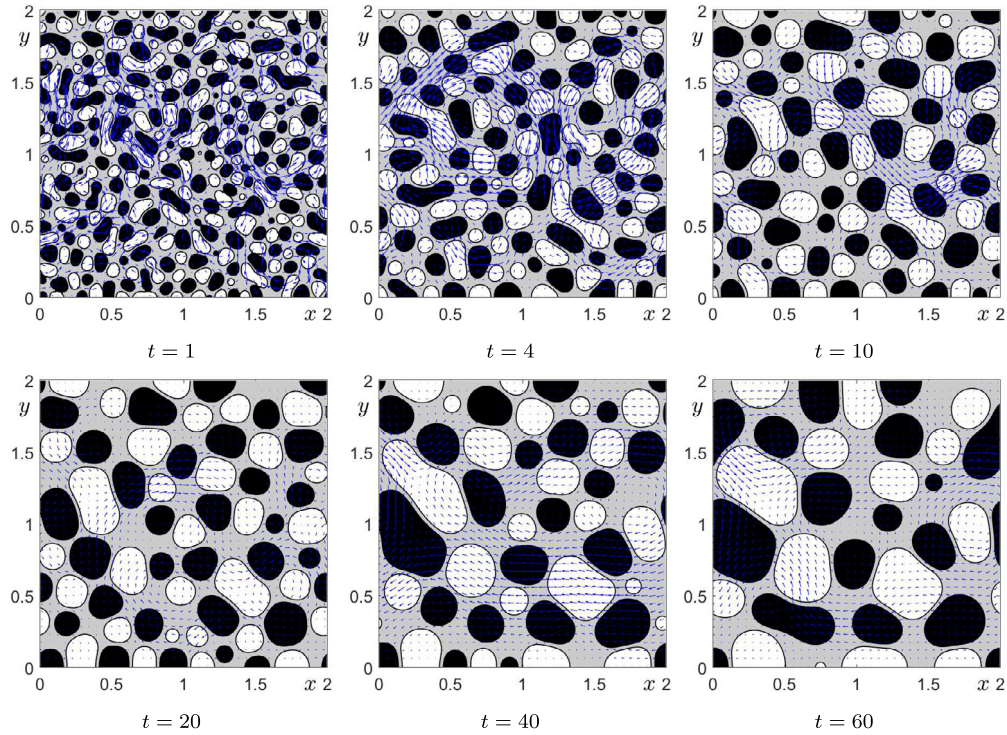
Fig. 12. Snapshots of flow-coupled ternary phase separation with respect to $(\sigma_{12}, \sigma_{13}, \sigma_{23}) = (3, 1, 1)$.
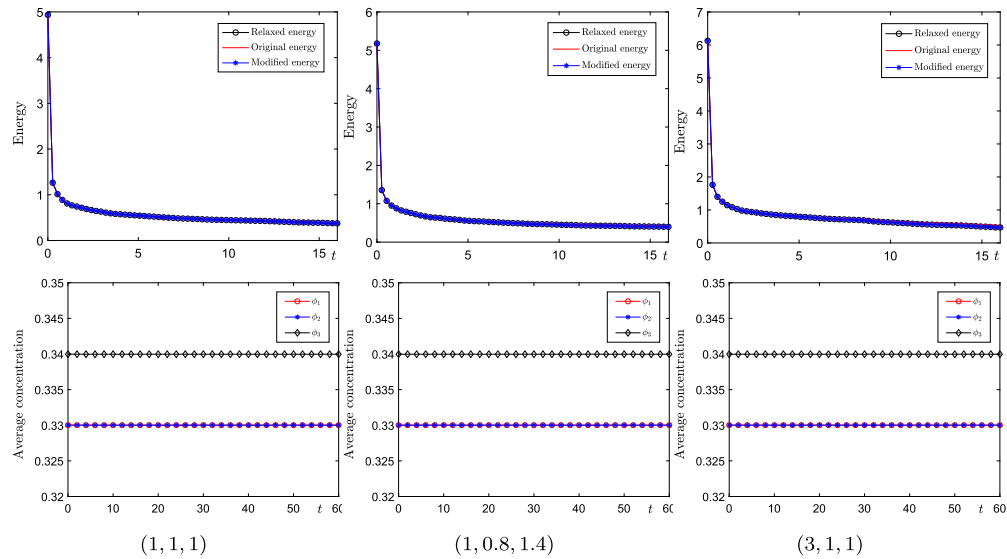
Fig. 13. Top and bottom rows show the evolutions of energy curves and average concentrations.
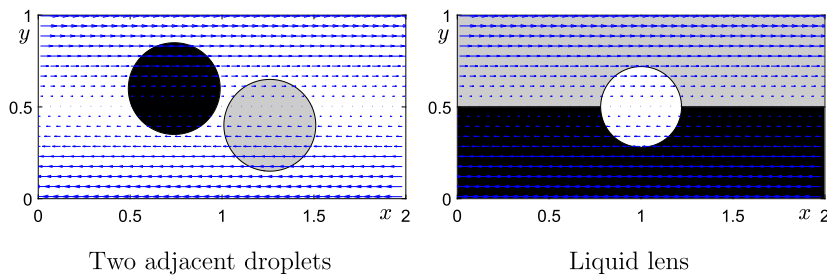
Fig. 14. Initial conditions of (a) two adjacent droplets and (b) liquid lens in simple shear flow.
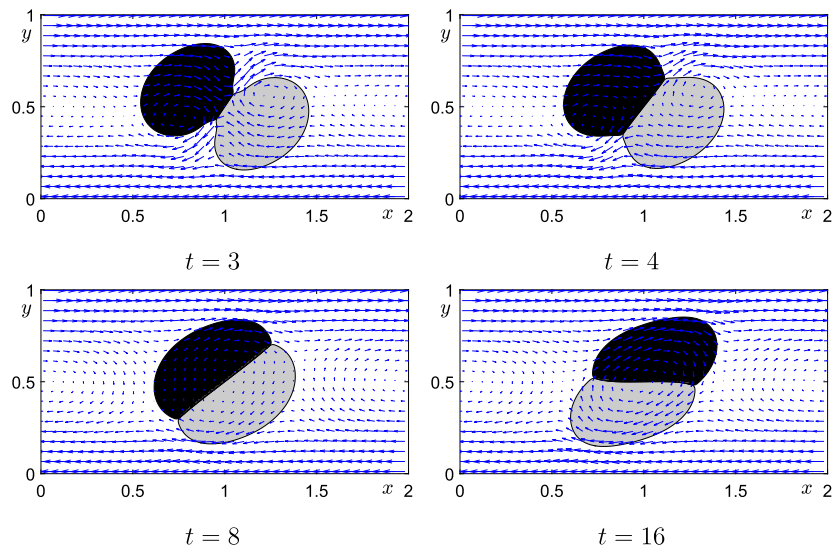
Fig. 15. Snapshots of two droplets in shear flow with respect to $(\sigma_{12}, \sigma_{13}, \sigma_{23}) = (4, 4, 4)$.
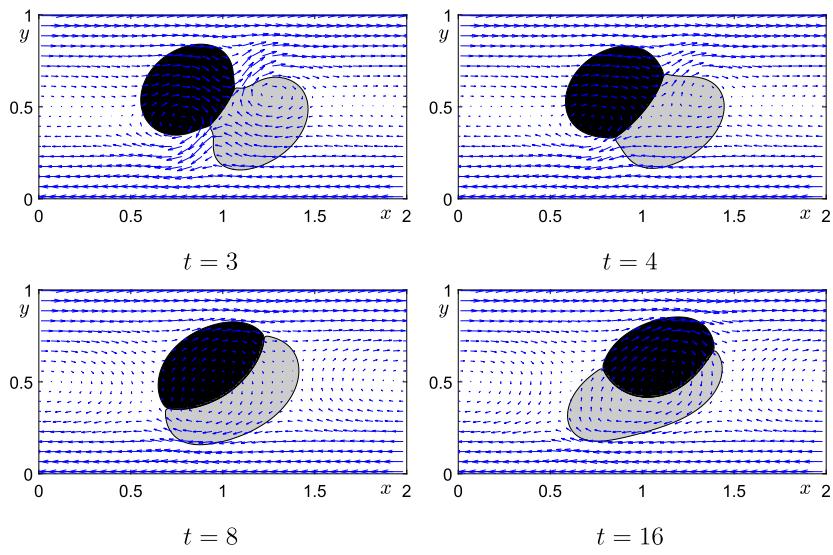
Fig. 16. Snapshots of two droplets in shear flow with respect to $(\sigma_{12}, \sigma_{13}, \sigma_{23}) = (4, 3.2, 5.6)$.
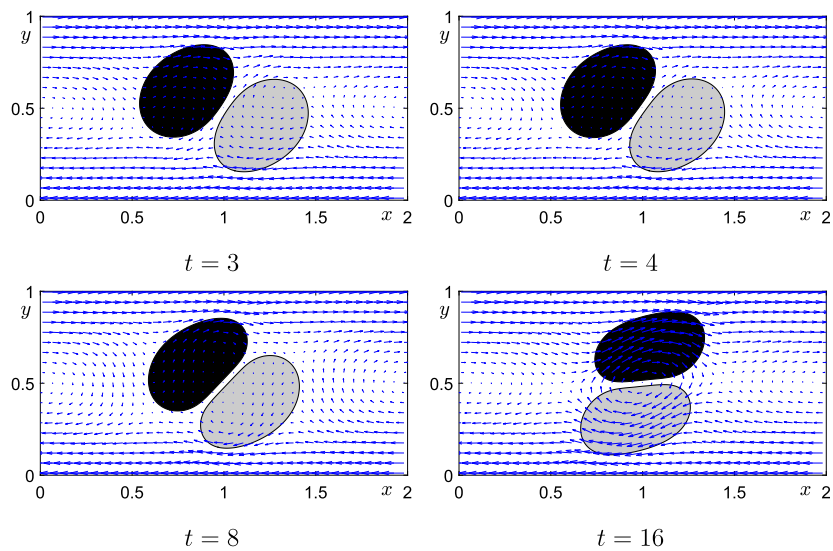
Fig. 17. Snapshots of two droplets in shear flow with respect to $(\sigma_{12}, \sigma_{13}, \sigma_{23}) = (12, 4, 4)$.
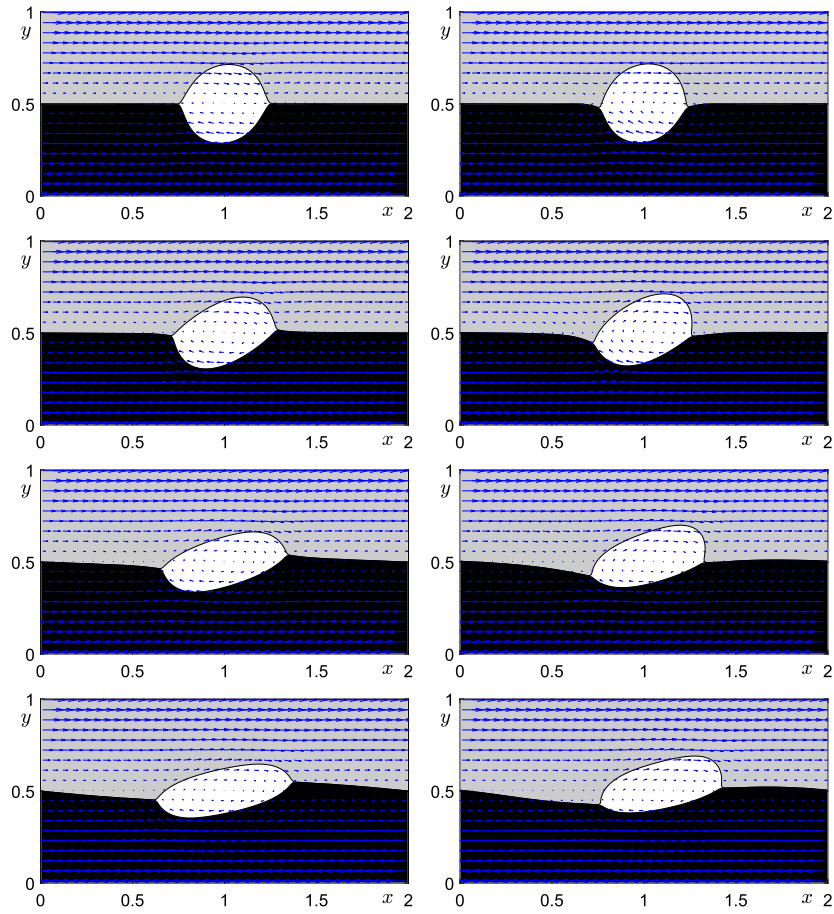
Fig. 18. Snapshots of the liquid lens in shear flow with respect to $(\sigma_{12}, \sigma_{13}, \sigma_{23}) = (4, 4, 4)$ (left) and $(4, 3.2, 5.6)$ (right). From top to bottom, the computational moments are $\Delta t = 0.6, \ 3, \ 8, \ 16$.

$$\phi_2(x, y, 0) = \frac{1}{2} + \frac{1}{2} \tanh\left(\frac{y - 3}{\epsilon}\right), \tag{98}$$

$$\phi_3(x, y, 0) = 1 - \phi_1(x, y, 0) - \phi_2(x, y, 0), \tag{99}$$

$$u(x, y, 0) = v(x, y, 0) = 0, \ p(x, y, 0) = 0. \tag{100}$$

Here, the parameters are set as $\Delta t = 0.001$, $\epsilon = 0.018$, $M = 0.1$, $Re = 30$, $g = 10$, $S = 30$, and $(\sigma_{12}, \sigma_{13}, \sigma_{23}) = (1, 1, 1)$. The density ratio is $\rho_1 : \rho_2 : \rho_3 = 3 : 1 : 2$ is used. Fig. 20 displays the snapshots of a 2D falling droplet in a ternary fluid system. The white, gray, and black regions are occupied by ϕ_1, ϕ_2, and ϕ_3, respectively. The velocities are represented by the blue arrows. We find that under the influence of gravity, the droplet deforms and falls. Owing to the impact of the droplet, the cavity appears. After the droplet completely penetrates the interface, the cavity phenomenon generally vanishes because of the effect of the surface tension.

Next, we perform the corresponding 3D simulation in the domain $\Omega = (0, 2) \times (0, 2) \times (0, 4)$. The mesh size $128 \times 128 \times 256$ is used. The initial conditions are defined as follows:

$$\phi_1(x, y, z, 0) = \frac{1}{2} + \frac{1}{2} \tanh\left(\frac{0.25 - \sqrt{(x - 1)^2 + (y - 1)^2 + (z - 3.4)^2}}{\epsilon}\right), \tag{101}$$

$$\phi_2(x, y, z, 0) = \frac{1}{2} + \frac{1}{2} \tanh\left(\frac{z - 3}{\epsilon}\right), \tag{102}$$

$$\phi_3(x, y, z, 0) = 1 - \phi_1(x, y, z, 0) - \phi_2(x, y, z, 0), \tag{103}$$

$$u(x, y, z, 0) = v(x, y, z, 0) = 0, \ p(x, y, z, 0) = 0. \tag{104}$$

The other parameters remain unchanged. Fig. 21 displays the snapshots of a 3D falling droplet in a ternary fluid system. The black region is occupied by ϕ_1. We find that the droplet deforms and eventually penetrates the interface. The simulations indicate that the proposed time-marching method can be effectively applied to the three-component fluid system under the combined effects of gravity and surface tension.

5. Discussions

In this study, we developed linear, second-order accurate, and consistently stable schemes for an immiscible fluid flow-coupled ternary CH system. It should be noted that the mixing of miscible fluids is common in industrial fields. Through the liquid/liquid interface, the
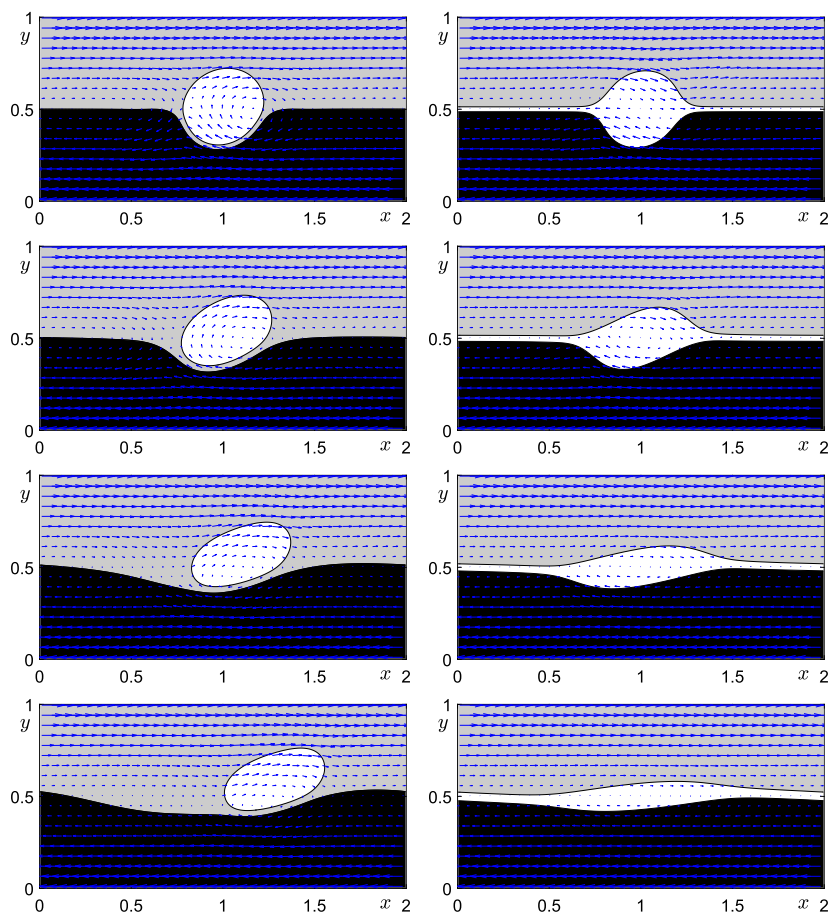
Fig. 19. Snapshots of the liquid lens in shear flow with respect to $(\sigma_{12}, \sigma_{13}, \sigma_{23}) = (4, 4, 12)$ (left) and $(12, 4, 4)$ (right). From top to bottom, the computational moments are $\Delta t = 0.6, \ 3, \ 8, \ 16$.

interpenetration of different fluids reflect the miscible property. Xie and Vorobev [65] developed a phase-field model to describe multi-phase miscible fluids by adopting a modified CH-type equation. In their work, the mass concentration was represented by a phase-field function $C \in [0, 1]$. By considering the case with equal surface tension for each component, the evolutionary equation derived from a Fick's law can be expressed as

$$\frac{\partial C}{\partial t} + \nabla \cdot (C\mathbf{u}) = M\Delta\mu, \tag{105}$$

where $\mu = \mu_0 + Gry - Ca\Delta C$. Here, $\mu_0 = df_0/dC$, Gr is the Grashof number, Ca is the capillary number, and y is the vertical coordinate in 2D space [65]. The free energy functional is

$$f_0 = \frac{3}{4}\left[\left(\frac{1}{2}+C\right)\ln\left(\frac{1}{2}+C\right) + \left(\frac{1}{2}-C\right)\ln\left(\frac{1}{2}-C\right)\right] - \left(\frac{3}{2}-A\right)C^2,$$

where A is a thermodynamic parameter [65]. The term Gry represents the barodiffusion. If we consider $Gr = 0$, then the pure diffusion state is recovered. For Eq. (105) that describes the miscible fluid boundary, our proposed scheme can be directly applied by defining the appropriate auxiliary variable related to the free energy. In the actual computation, the nonlinear term was treated in an explicit manner, and a similar stabilization parameter was introduced to suppress the stiffness. The present study focused on an efficient time-marching method for ternary immiscible fluids. The extension to multi-phase miscible fluids will be investigated in future research.

6. Conclusions

For the purposes of the discrete energy dissipation law and efficient numerical implementation, we proposed second-order time-accurate, linearly implicit-explicit methods for a ternary CH fluid system based on a modified version of the SAV approach. An efficient and effective energy relaxation method was used to enhance the consistency between the original and modified energies. At each time step, only the totally decoupled elliptic equations with constant coefficients needed to be solved. The unique solvability and discrete energy stability of the proposed methods were strictly estimated. The numerical experiments showed that the proposed schemes satisfied the expected accuracy and unconditional energy dissipation properties. The relaxed and original energy curves were in good agreement. Furthermore, the proposed method effectively simulated hydrodynamically coupled phase separation, droplet dynamics in shear flow, liquid lenses, and falling droplets. In future studies, the proposed schemes will be extended to simulate incompressible multi-component fluid flows with heat conductivity [66]. The C codes of typical numerical examples can be found at http://github.com/yang521.
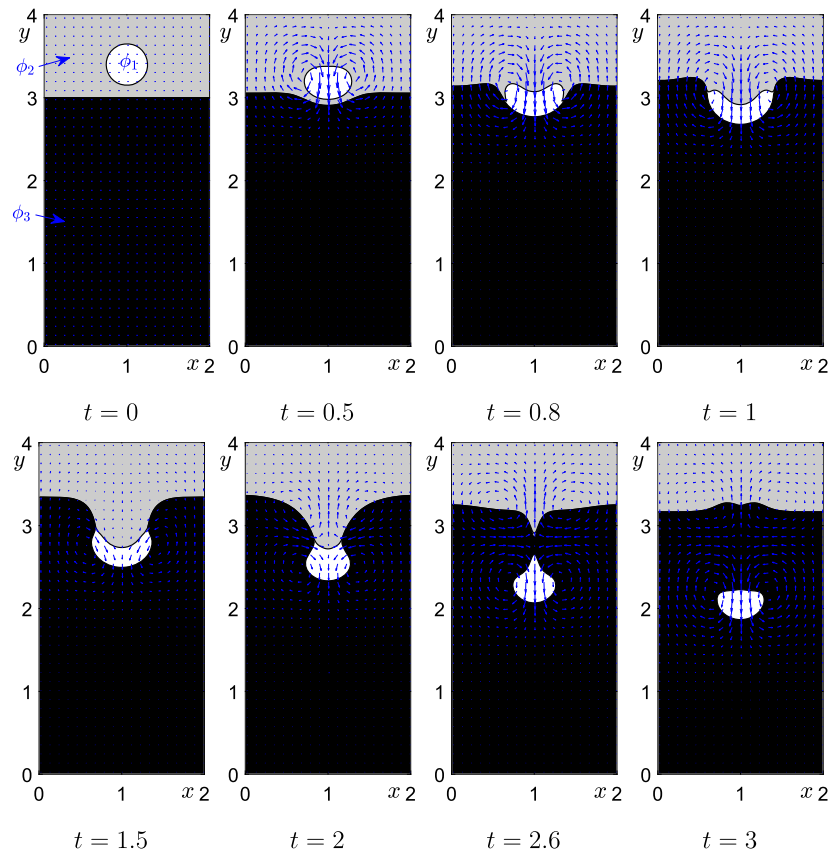
Fig. 20. Snapshots of 2D falling droplet in a ternary fluid system. The computational moments are shown under each figure.
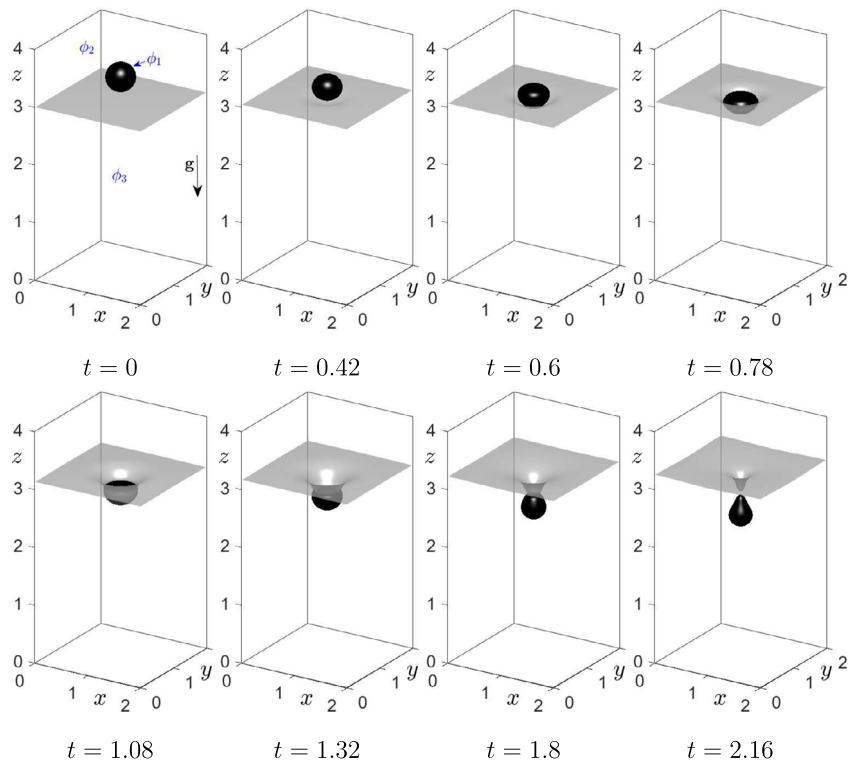
Fig. 21. Snapshots of 3D falling droplet in a ternary fluid system. The computational moments are shown under each figure.

Declaration of competing interest

The authors declare that they have no known competing financial interests or personal relationships that could have appeared to influence the work reported in this paper.

Data availability

Data will be made available on request.

Acknowledgement

References

[1] A. Zhang, J. Du, Z. Guo, Q. Wang, S. Xiong, Commun. Comput. Phys. 267 (2021) 108042.
[2] Y. Li, Q. Xia, S. Yoon, C. Lee, B. Lu, J. Kim, Commun. Comput. Phys. 264 (2021) 107956.
[3] J. Kim, H.G. Lee, Commun. Comput. Phys. 221 (2017) 102–108.
[4] J.W. Cahn, J.E. Hilliard, J. Chem. Phys. 28 (1948) 258–267.
[5] J. Kim, Commun. Comput. Phys. 12 (2012) 613–661.
[6] Y. Palzhanov, A. Zhiliakov, A. Quaini, M. Olshanskii, Comput. Methods Appl. Mech. Eng. 387 (2021) 114167.
[7] M. Sohaib, A. Shah, Commun. Nonlinear Sci. Numer. Simul. 112 (2022) 106547.
[8] K.A. Yuana, B. Jalaali, E.P. Budiana, Pranowo, A. Widyaparaga, Indarto, Deendarlianto, Eur. J. Mech. B, Fluids 85 (2021) 276–288.
[9] Q. Xia, Q. Yu, Y. Li, Comput. Methods Appl. Mech. Eng. 384 (2021) 113987.
[10] Y. Li, J. Wang, B. Lu, D. Jeong, J. Kim, Pattern Recognit. 93 (2019) 124–133.
[11] M. Zhang, G.-F. Zhang, Comput. Math. Appl. 102 (2021) 1–14.
[12] S. Zhou, Y.M. Xie, Int. J. Mech. Sci. 198 (2021) 106349.
[13] M. Ebenbeck, H. Garcke, SIAM J. Numer. Anal. (2019), https://doi.org/10.1137/18M1228104.
[14] S. Lee, Bull. Math. Biol. 80 (2) (2018) 583–597.
[15] S. Lee, J. Shin, Comput. Math. Appl. 77 (1) (2019) 189–198.
[16] J. Shin, H.G. Lee, J.-Y. Lee, J. Comput. Phys. 347 (6) (2017) 367–381.
[17] J. Guo, C. Wang, S.M. Wise, X. Yue, Commun. Math. Sci. 14 (2) (2016) 489–515.
[18] L. Dong, C. Wang, S.M. Wise, Z. Zhang, J. Comput. Phys. 442 (2021) 110451.
[19] K. Cheng, W. Feng, C. Wang, S.M. Wise, J. Comput. Appl. Math. 362 (2019) 574–595.
[20] Q. Du, L. Ju, X. Li, Z. Qiao, J. Comput. Phys. 363 (2018) 39–54.
[21] L. Wang, H. Yu, J. Sci. Comput. 77 (2018) 1185–1209.
[22] J. Kou, S. Sun, X. Wang, SIAM J. Sci. Comput. 42 (2020) B30–B56.
[23] J. Yang, J. Kim, Commun. Comput. Phys. 261 (2021) 107825.
[24] M. Sun, X. Xiao, X. Feng, K. Wang, Comput. Methods Appl. Mech. Eng. 390 (2022) 114450.
[25] M. Sun, X. Feng, K. Wang, Comput. Methods Appl. Mech. Eng. 367 (2020) 113123.
[26] Q. Li, L. Mei, Commun. Comput. Phys. 260 (2021) 107290.
[27] C. Zhang, J. Ouyang, C. Wang, S.M. Wise, J. Comput. Phys. 423 (2020) 109772.
[28] K. Mu, H. Ding, T. Si, Phys. Fluids 32 (2020) 042103.
[29] G. Zhu, J. Kou, J. Yao, A. Li, S. Sun, J. Comput. Phys. 405 (2020) 109170.
[30] J. Yang, Z. Tan, J. Kim, J. Comput. Phys. 452 (2022) 110909.
[31] J. Kim, Comput. Methods Appl. Mech. Eng. 196 (45–48) (2007) 4779–4788.
[32] J. Kim, Comput. Methods Appl. Mech. Eng. 198 (2009) 3105–3112.
[33] H.G. Lee, J. Kim, Eur. J. Mech. B, Fluids 42 (2013) 37–46.
[34] C.-Y. Zhang, H. Ding, P. Gao, Y.-L. Wu, J. Comput. Phys. 309 (2016) 37–51.
[35] H.-R. Liu, P. Gao, H. Ding, J. Comput. Phys. 348 (2017) 45–65.
[36] H.-L. Li, H.-R. Liu, H. Ding, J. Comput. Phys. 420 (1) (2020) 109709.
[37] H.G. Lee, J.-W. Choi, J. Kim, Physica A 391 (2012) 1009–1019.
[38] Y. Li, R. Liu, Q. Xia, C. He, Z. Li, J. Comput. Appl. Math. 401 (2022) 113778.
[39] F. Boyer, C. Lapuerta, ESAIM: Math. Model. Numer. Anal. 40 (2006) 653–687.
[40] H. Liang, B.C. Shi, Z.H. Chai, Phys. Rev. E 93 (2016) 013308.
[41] R. Kalantarpour, A. Ebadi, S.M. Hosseinalipour, H. Liang, Comput. Fluids 204 (2020) 104480.
[42] H. Liang, J. Xu, J. Chen, Z. Chai, B. Shi, Appl. Math. Model. 73 (2019) 487–513.
[43] W. Chen, C. Wang, S. Wang, X. Wang, S.M. Wise, J. Sci. Comput. 84 (2020) 27.
[44] J. Zhang, X. Yang, J. Comput. Phys. 404 (2020) 109115.
[45] J. Yang, J. Kim, Commun. Nonlinear Sci. Numer. Simul. 102 (2021) 105923.
[46] J. Yang, J. Chen, Z. Tan, Eng. Comput. (2022), https://doi.org/10.1007/s00366-022-01618-5.
[47] C-Y. Zhang, H. Ding, P. Gao, Y-L. Wu, J. Comput. Phys. 309 (2016) 37–51.
[48] M. Jiang, Z. Zhang, J. Zhao, J. Comput. Phys. 456 (2022) 110954.
[49] Y. Zhang, J. Shen, J. Comput. Phys. 464 (2022) 111311.
[50] M.O. Deville, P.F. Fischer, E.H. Mund, High-Order Methods for Incompressible Fluid Flow, vol. 9, Cambridge University Press, 2002.
[51] W. Chen, Y. Liu, C. Wang, S. Wise, Math. Comput. 85 (2016) 2231–2257.

[52] Y. Liu, W. Chen, C. Wang, S. Wise, Numer. Math. 135 (2017) 679–709.
[53] W. Chen, W. Feng, Y. Liu, C. Wang, S. Wise, Discrete Contin. Dyn. Syst., Ser. B 24 (2019) 149–182.
[54] A. Diegel, C. Wang, X. Wang, S. Wise, Numer. Math. 135 (2017) 495–534.
[55] M. Yuan, W. Chen, C. Wang, S. Wise, Z. Zhang, J. Sci. Comput. 87 (2021) 78.
[56] J. Shen, J. Xu, SIAM J. Numer. Anal. 56 (5) (2018) 2895–2912.
[57] X. Li, J. Shen, H. Rui, Math. Comput. 88 (2019) 2047–2068.
[58] M. Wang, Q. Huang, C. Wang, J. Sci. Comput. 88 (2) (2021) 33.
[59] Q. Cheng, C. Wang, Adv. Appl. Math. Mech. 13 (6) (2021) 1318–1354.
[60] X. Yang, Comput. Methods Appl. Mech. Eng. 376 (2021) 113589.
[61] U. Trottenberg, C. Oosterlee, A. Schüller, Multigrid, Academic Press, New York, 2001.
[62] J. Kim, J. Comput. Phys. 204 (2005) 784–804.
[63] H.G. Lee, J. Kim, Physica A 423 (2015) 33–50.
[64] H.G. Lee, J. Kim, J. Eng. Math. 75 (2012) 15–27.
[65] R. Xie, A. Vorobev, J. Colloid Interface Sci. 464 (2016) 48–58.
[66] X. Pan, C. Lee, J.-I. Choi, J. Comput. Phys. 369 (2018) 191–208.